








RESEARCH ARTICLE

Aircraft observations and sub-km modelling of the lake–land breeze circulation over Lake Victoria

Beth J. Woodhams¹  | Paul A. Barrett²  | John H. Marsham^{1,3}  |
Cathryn E. Birch¹  | Caroline L. Bain²  | Jennifer K. Fletcher^{1,3}  |
Andrew J. Hartley²  | Stuart Webster² | Solomon Mangeni⁴

¹Institute for Climate and Atmospheric Science, School of Earth and Environment, University of Leeds, Leeds, UK

²Met Office, Exeter, UK

³National Centre for Atmospheric Science, University of Leeds, Leeds, UK

⁴Uganda National Meteorological Authority, Kampala, Uganda

Correspondence

B. J. Woodhams, Institute for Climate and Atmospheric Science, School of Earth and Environment, University of Leeds, Leeds LS2 9JT, UK.

Email: b.j.woodhams@leeds.ac.uk

Funding information

UK National Centre for Atmospheric Science; UK Met Office; UKAID through WISER HIGHWAY project; GCRF African SWIFT, Grant/Award Number: NE/P021077/1; Future Climate for Africa (FCFA) HyCRISTAL, Grant/Award Number: NE/M019985/1; NERC SPHERES DTP, Grant/Award Number: NE/L002574/1; NERC/GCRF ACREW, Grant/Award Number: NE/R000034/1

Abstract

The lake–land breeze circulation over Lake Victoria was observed in unprecedented detail with a research aircraft during the HyVic pilot flight campaign in January 2019. An evening and morning flight observed the lake and land breezes respectively under mostly dry conditions. The circulation was observed at various heights along a transect across the lake and onshore in Tanzania. Profiles of the lower troposphere were recorded by dropsondes over the lake and land. Convection-permitting MetUM simulations with different horizontal grid-spacings (including sub-km) were run for the flight periods. During the evening flight, the aircraft crossed the lake breeze front over land at 1627 LT, approximately 50 km to the east of the lake shore, recording a $6 \text{ g}\cdot\text{kg}^{-1}$ decrease in specific humidity and reversal in wind direction over ~ 5 km. During the morning flight, a shallow land breeze was observed across the eastern shore at 0545 LT. At least one region of increased and deeper moisture (previously seen in simulations but never observed) was sampled over the lake surface between 0527 and 0855 LT. This bulge of moisture was likely formed from the lifting of near-surface moist air above the lake by low-level convergence. The observations and model simulations suggest that low-level convergence occurred at the leading edge of the land breeze, which had detached from the main land breeze and independently propagated westward across the lake with wave-like characteristics. The MetUM simulations were able to reasonably reproduce the lake breeze front, bulge feature, and its propagation, which is a major achievement given the sparse observational data for model initialisation in this region. However, some timing, resolution and boundary-layer depth biases require further investigation. Overall, this pilot campaign provided an unprecedented snapshot of the Lake Victoria lake–land breeze circulation and motivates a more comprehensive field campaign in the future.

KEYWORDS

East Africa, Lake Victoria, lake–land breeze circulation, observations, research aircraft

This is an open access article under the terms of the Creative Commons Attribution License, which permits use, distribution and reproduction in any medium, provided the original work is properly cited.

© 2021 Crown copyright. Quarterly Journal of the Royal Meteorological Society published by John Wiley & Sons Ltd on behalf of Royal Meteorological Society. This article is published with the permission of the Controller of HMSO and the Queen's Printer for Scotland.

1 | INTRODUCTION

Lake–land breeze circulations, which are similar to sea breeze circulations, have a significant influence on the weather and climate of lakes and their surroundings. Lake breezes can produce convergence and trigger convection, leading to intense rainfall inland (e.g., Okeyo, 1986; Alexander *et al.*, 2018; Wang *et al.*, 2019). Convergent land breezes from opposite sides of the lake enhance rainfall over the lakes themselves (e.g., Thiery *et al.*, 2015; Woodhams *et al.*, 2019; Zou *et al.*, 2020) and are important in the formation of Great Lakes snow storms (e.g., Passarelli and Braham, 1981; Ballentine, 1982; Steenburgh *et al.*, 2000). These circulations also affect air quality along shorelines (e.g., Sills *et al.*, 2011).

The timing, depth and horizontal extent of lake–land breezes are affected by various factors, including: temperature or sensible heat flux gradients (e.g., Biggs and Graves, 1962; Segal *et al.*, 1997; Xu *et al.*, 2019; Purificação *et al.*, 2021); strength and direction of synoptic flow (e.g., Estoque, 1962; Simpson *et al.*, 1977; Arritt, 1993; Comer and McKendry, 1993; Laird *et al.*, 2001; Wang *et al.*, 2017; Wang *et al.*, 2019); stability (e.g., Mak and Walsh, 1976; Arritt, 1993; Crosman and Horel, 2012); size, depth and shape of the lake (e.g., Neumann and Mahrer, 1975; Physick, 1976; Segal *et al.*, 1997); height and slope of surrounding terrain (e.g., Wexler, 1946; Estoque, 1981; Estoque and Gross, 1981; Zumpfe and Horel, 2007); and roughness length of the surrounding land (e.g., Stivari *et al.*, 2003; Wang *et al.*, 2017). A thorough review of these factors is provided by Crosman and Horel (2010), with particular reference to numerical studies.

The depth of a lake breeze can vary from about 100 to 1,000 m (e.g., Lyons and Olsson, 1973; Comer and McKendry, 1993; Bischoff-Gauss *et al.*, 2006; Suresh, 2007; Kehler *et al.*, 2016; Iakunin *et al.*, 2018), but has been observed up to a maximum of 1,500 m (e.g., Stivari *et al.*, 2003; Asefi-Najafabady *et al.*, 2010). A return flow occurs approximately 1,000–2,000 m above the surface breeze (e.g., Moroz, 1967; Lyons, 1972; Keen and Lyons, 1978). Inland penetration of the lake breeze can be from several km to ~100 km in the literature cited above. The front of a sea (or lake or land) breeze marks the leading edge of the advected air and is generally associated with sharp gradients in temperature, moisture and wind, and a zone of convergence (Miller *et al.*, 2003; Sills *et al.*, 2011). The width of the lake breeze front (LBF) in the offshore direction is not as well studied; measurements from Lakes Michigan, Winnipeg and Manitoba showed the width to be less than 2 km (Lyons, 1972; Curry *et al.*, 2017), whereas Zumpfe and Horel (2007) estimated a width of 3–4 km for the smaller Great Salt Lake in northern USA. To some extent, the width will depend on the definition, which can

be the width of the region over which convergence occurs, or the width over which temperature, moisture and wind show the greatest change.

Discussion of land–lake breezes is largely neglected in the literature, especially over lakes where two land breezes may oppose one another from opposite shores. Land breezes tend to be weaker than their lake (or sea) counterparts (Mak and Walsh, 1976) and have been shown to enhance cloudiness or convection over a lake during the early morning as a result of convergence and likely thermal instability above the warm surface (e.g., Neumann and Mahrer, 1975; Physick, 1976; Keen and Lyons, 1978; Pielke and Segal, 1986; Comer and McKendry, 1993; Tsujimoto and Koike, 2013; Koseki and Mooney, 2019; Xu *et al.*, 2019).

Lake Victoria in East Africa (Figure 1) is the largest tropical lake in the world, where storms and high winds, thought to be largely driven by nocturnal land breezes, are estimated to contribute to 5,000 fatalities on the lake every year (Cannon *et al.*, 2014). An estimated 3.5 million people rely on the lake for their livelihoods, including 200,000 who fish on the lake (Semazzi, 2011). The lake also supports transport and trade routes, as well as hydroelectric power. Flohn and Fraedrich (1966) noted the existence of a diurnal circulation system and linked the early morning maximum of rainfall over the lake to convergence produced by the nocturnal land breeze. Conversely, a divergent lake breeze suppresses convection over the lake, and uplift and moist lake air at the LBF favour convective initiation over land during the day (e.g., Datta, 1981; Ba and Nicholson, 1998; Thiery *et al.*, 2015; Woodhams *et al.*, 2019). The lake and land breezes are also reinforced by anabatic and katabatic flows respectively, especially on the steep slopes of the eastern branch of the East African Rift (Lumb, 1970; Okeyo, 1986; Mukabana and Pielke, 1996; Anyah *et al.*, 2006; Thiery *et al.*, 2015). Van de Walle *et al.* (2020) showed that convergence over the lake at night is enhanced in the north–south direction by the deflection of the easterly prevailing winds around the eastern branch of the East African Rift in stable conditions.

Most previous studies of Lake Victoria's lake–land breeze circulation have analysed the mean diurnal cycle of winds, moisture and precipitation, thereby neglecting the impact of daily variability, and smoothing out small-scale details (e.g., Mukabana and Pielke, 1996; Song *et al.*, 2004; Anyah *et al.*, 2006; Thiery *et al.*, 2015; Camberlin *et al.*, 2018). For the first time, Woodhams *et al.* (2019, hereafter W19) investigated individual case-studies of the lake–land breeze circulation and storm events over Lake Victoria using a convection-permitting (CP) version of the Met Office Unified Model (MetUM) with 1.5 km horizontal grid-spacing. The study included simulations of a dry period in July, a large storm during May (Long Rains season) and a smaller storm from July (dry season). All W19

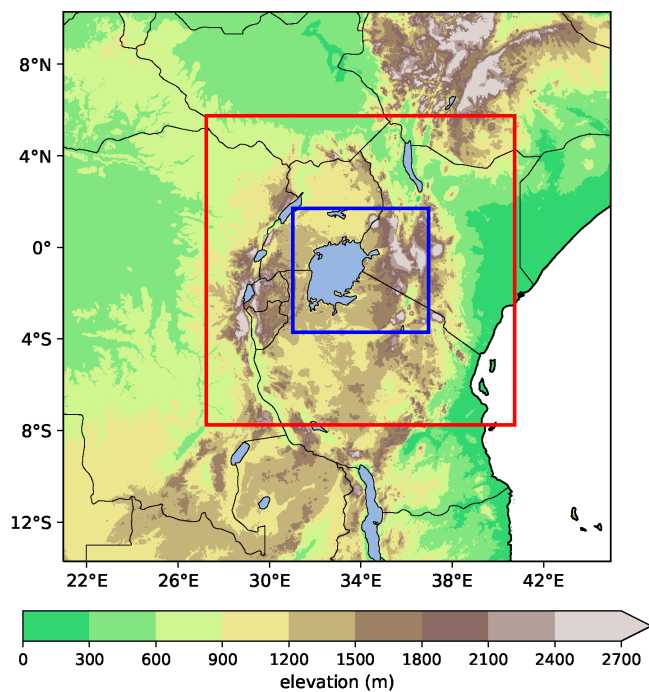


FIGURE 1 Elevation data from the Global Land One-kilometer Base Elevation (GLOBE) Digital Elevation Model (Hastings and Dunbar, 1999). Full domain, red box and blue box correspond to 4.4 km, 1.5 km and 300 m nests respectively for CP MetUM runs during the HyVic period [Colour figure can be viewed at wileyonlinelibrary.com]

simulations showed the formation of lake breezes across the shorelines of Lake Victoria (their figure 14), with convergence generally strongest to the east of the lake, where the lake breeze runs into the prevailing easterly winds (also Mahony *et al.*, 2021). In the W19 dry case, the lake breeze across the eastern shore occurred over a depth of ~ 1 km (their figures 7c,i,o). The LBF reached its maximum extent inland (80 km) at 1800 LT (local time, LT = UTC+3 hr) and was associated with enhanced upward motion and the transport of moist air aloft. A return flow was identified between ~ 2 and 5 km amsl (~ 1 –4 km agl),¹ which advected the moist air back toward the lake and induced subsidence over the lake surface (also shown in Thiery *et al.*, 2015). A return flow also occurred to the east of the LBF – manifested in a reduction in the prevailing easterlies in the mid-levels – resulting in divergent flow above the LBF.

In the W19 dry case, the convergence line to the east of the lake propagated westward back toward and across the lake between 2200 and 0900 LT, initially driven by the formation of a land breeze in the lowest few hundred metres across the eastern shore and later, at 0200 LT, by the strengthening of the prevailing near-surface easterly

flow (their figures 7d–f,j–l,p–r and 14). This propagation showed that – at least in the W19 case – the daytime convergence over land and nocturnal convergence over the lake were the same feature. In the Long Rains (March–May) case-study, this propagation was shown to be responsible for the lakeward propagation of a storm which formed at the eastern LBF.

The land breeze density current across the eastern shore in the W19 dry period collided with stable air in the lowest few hundred metres above the lake surface, causing the moist near-surface air to be lofted upward into a shallow bulge. This bulge had a depth of a few hundred metres and propagated westward with the convergence (their figures 7d–f,j–l). A shallow land breeze also formed across the western shore around 0200 LT, which reinforced the convergence over the lake. The centre of the moisture bulge was located over the centre of the lake at 0200 LT and over the western shore by 0900 LT (W19, their figures 7k and l, respectively). W19 hypothesised that the properties of this moisture bulge (moisture content and depth) could determine whether or not a storm initiates over the lake itself. This type of feature has not been described in any previous literature on land breezes.

Despite the importance of accurate and timely weather information for the lake, forecasting severe weather in this region remains a great challenge for numerical weather prediction (NWP) models. The introduction of a CP forecast model over East Africa by the UK Met Office (Chamberlain *et al.*, 2014; Woodhams *et al.*, 2018; Hanley *et al.*, 2021) has improved the diurnal cycle of rainfall and representation of convective storms compared to forecasts from the global operational system, but biases in rainfall timing and amount persist and overall forecast skill remains low. Likely reasons for poor model skill include unknown, unquantified, or unresolved trigger mechanisms and a lack of observations – especially upper air – for data assimilation.

Given the lack of *in situ* observations in the region, the processes and features described in W19 (and most other studies) were based almost entirely on model simulations. Existing *in situ* observations of the lake–land breeze circulation have been obtained from weather stations with fixed locations (e.g., Lumb, 1970; Datta, 1981), but it is difficult to use them in isolation to build a full picture of the circulation, especially if the recording frequency is low. In addition, such stations can only sample the circulation at the surface. Upper-air observations are particularly lacking in the region, and observations over the lake itself present an exceptional challenge. As such, the vertical structure of the lake and land breezes and a possible moisture bulge over Lake Victoria have not been observed.

In January 2019, the HyVic pilot flight campaign took place, observing the lake–land breeze circulation over

¹amsl = above mean sea level; agl = above ground level

Lake Victoria using the UK's BAe-146-301 Atmospheric Research Aircraft operated by the FAAM (Facility for Airborne Atmospheric Measurements) Airborne Laboratory. The flights aimed to investigate some of the features simulated by the model in the dry case in W19 (such as the moisture bulge); characterise the lake and land breeze fronts; and collect observations to be used for model verification. CP MetUM simulations, including at sub-km resolution, were run during the campaign period. The campaign consisted of an evening and morning flight, both with a duration of approximately 4 hr, to sample the lake and land breeze components of the circulation respectively. The flights took place during a period with very little rainfall, therefore without the presence of a major storm to complicate the flows and analysis. Although observations of storms would be very interesting, the aircraft is not able to fly in such conditions. However, it is beneficial to gain an initial understanding of the lake–land breeze system for a case without much deep moist convection, before considering complex interactions between the lake–land circulations and moist convection. Also, other than an overall higher specific humidity and the resulting effects of the presence of the storm, the lake–land breeze circulation during the Long Rains case from W19 showed remarkable similarities to their dry case (their figures 12 and 13), showing that a dry period can still offer insight into rainfall occurrence over the lake. Given the high seasonal and sub-seasonal variability in moisture availability and circulation in the region (e.g., Yang *et al.*, 2015; W19), it is noted that the two flights presented in this paper cannot be used to draw robust conclusions about the lake–land breeze circulation on all days. However, this novel set of observations can still provide a snapshot of the lake–land breeze circulation in unprecedented detail, be used for detailed evaluation of model performance, and inform future field campaigns.

This short campaign was designed as an add-on to the MOYA campaign based in Entebbe, Uganda (measuring methane over tropical Africa; Barker *et al.*, 2020) and was a pilot for a more comprehensive campaign in the future. The campaign was also associated with the HIGHWAY field campaign, which included two enhanced observation periods during March–May and July–August 2019. Among other data sources, observations were collected using ground-based weather stations across the basin and radar located on the southern shore of the lake in Mwanza, Tanzania (Waniha *et al.*, 2019). HIGHWAY has also enhanced the long-term collection of atmospheric data over East Africa to improve the quality of operational forecasts and increase climate monitoring.

The HyVic pilot flight campaign flight tracks and observations are introduced in Section 2, along with other observational data and accompanying model simulations.

Section 3.1 gives an overview of the synoptic conditions during the campaign and Sections 3.2 and 3.3 present and discuss the observations from the evening and morning flights respectively, alongside the model simulations. The model is evaluated in Section 3.4. Conclusions are drawn in Section 4, including suggestions for an extended field campaign in the future.

2 | METHODS

2.1 | Flights

This study was performed using the FAAM BAe-146 aircraft, operating out of Entebbe, Uganda (white star, Figures 2a,c) on 26–27 January 2019. The campaign consisted of two flights: one in the evening to observe the lake breeze, and one the following morning to observe the land breeze. Given the lack of previous observational data, much of the flight planning was based on the dry period simulation in W19. Since the W19 case-study was taken from July, forecast data from the 4.4 km Met Office operational Tropical Africa model (Hanley *et al.*, 2021) for January and February 2018 were also used to inform the flight plans. However, the operational data were on a coarser grid and had reduced model output times and variables compared to the simulations in W19.

It was important that the morning flight directly followed the evening flight; W19 showed that onshore convergence to the east of the lake during the evening can propagate across the lake overnight, therefore the same ‘system’ could be sampled in both flights. The flights were timed to sample the mature lake and land breezes, whilst also taking into account constraints on aircraft and crew turnaround between flights, and the minimum safe altitude when flying in the dark. For safety reasons, flights could only take place when there were no significant storms. Flight times are summarised in Table 1.

Both flights were based along an approximately northwest to southeast transect between Entebbe (on the northwest shore of the lake) and approximately 130 km onshore from the eastern shore in Tanzania (Figure 2). The bearing of this transect is $\sim 120^\circ$, such that it is approximately west to east, but with a slight north to south component. For the remainder of the paper, ‘westerly’ and ‘easterly’ will be used to describe along-transect winds, but the reader should bear in mind that these descriptions are approximate. This transect was flown at several altitudes in order to observe the lake and land breezes in two dimensions. During both flights, six sondes were dropped from the highest leg of the transect to obtain full profiles throughout the lower troposphere. The aircraft transect was chosen to be similar to the model transect analysed in W19, whilst

FIGURE 2 (a, c) Map view of flight tracks (coloured lines) with terrain height (shading, as in Figure 1) and mean 10 m wind vectors from ERA5 during the flight duration. The white star marks Entebbe airport. (b, d) Cross-section view of the flight tracks (coloured lines) and dropsonde profiles (black lines). Red numbers show distance in km from the eastern shore of the lake. Colours along the flight tracks show the time of day. (a, b) show the evening flight and (c, d) the morning flight [Colour figure can be viewed at wileyonlinelibrary.com]

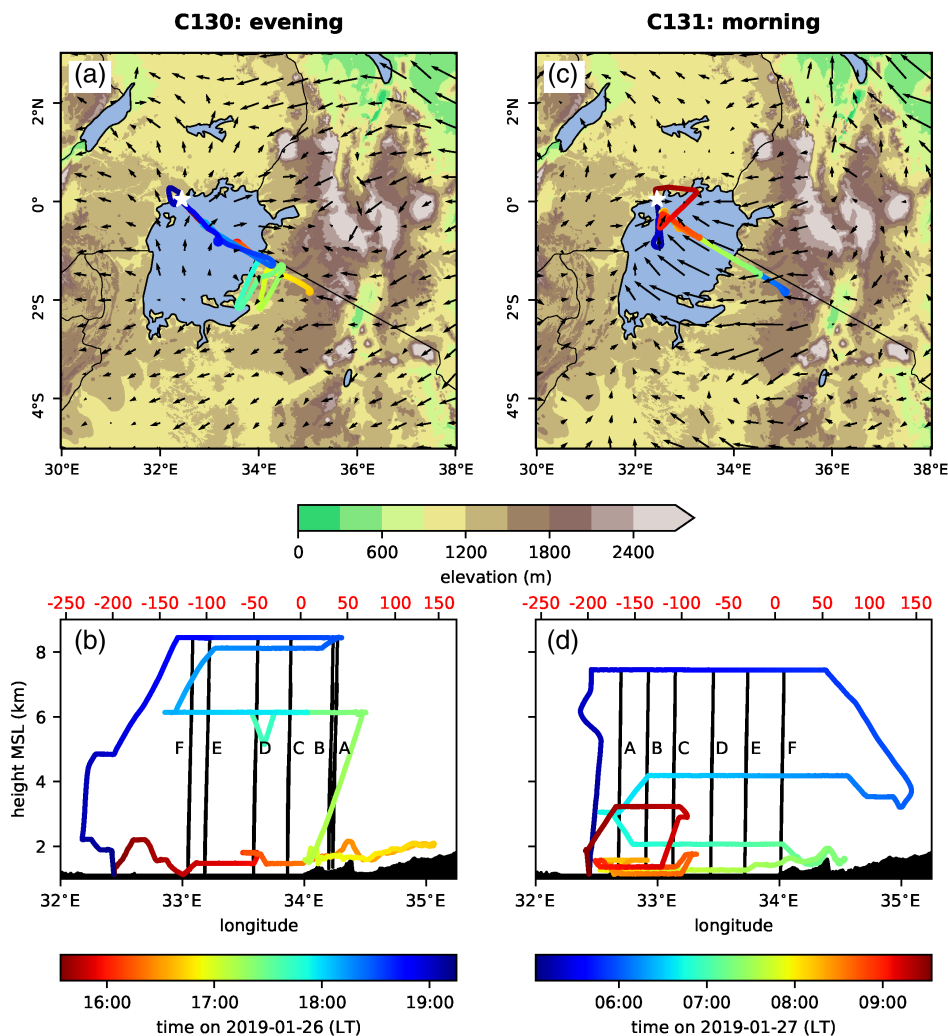


TABLE 1 A summary of the flights performed as part of the HyVic pilot flight campaign

Flight	Date	Takeoff	Landing	Entebbe sunset* or sunrise [†]
C130	26 January 2019	1234 UTC/1534 LT	1615 UTC/1915 LT	1606 UTC/1906 LT*
C131	27 January 2019	0208 UTC/0508 LT	0637 UTC/0937 LT	0359 UTC/0659 LT [†]

also choosing a navigable path over terrain to the east of the lake. Lake Victoria itself sits at 1,135 m amsl.

The evening flight began with a terrain-following leg at ~300 m agl (~1,450 m amsl over the lake; Figure 2a,b, red–orange colours), which passed from the lake onto the land to sample the lake breeze near to the surface. This leg was briefly interrupted over the lake (~33.6°) whilst awaiting air traffic control clearance. The low-level leg was followed by a return leg at ~6,000 m amsl (light blue colours) to sample the mid-level return flow. Between these along-transect legs, two legs were flown approximately perpendicular to the transect (parallel to the LBF; yellow–aqua colours) at the lower and upper altitudes. The aircraft then ascended to ~8,500 m amsl and dropped six

sondes from east to west, including two over land and four over the lake (Figure 2b, dark blue colours and Figure 3b, pink crosses). This flight pattern enabled low-level flying to take place in daylight with the dropsondes at dusk.

The morning flight began with the highest leg (~7,500 m amsl, dark blue colours, Figures 2c,d), along which six sondes were dropped from west to east, the first five over the lake and the final sonde just on the shoreline (Figures 2d and 3c, pink crosses). In this case, the highest leg was completed first due to altitude restrictions in the dark. The aircraft then performed two further legs at ~4,000 m (light blue colours) and ~2,000 m amsl (teal colours). As the latter leg reached the shoreline close to first light, the aircraft descended to ~300 m agl (~1,450 m

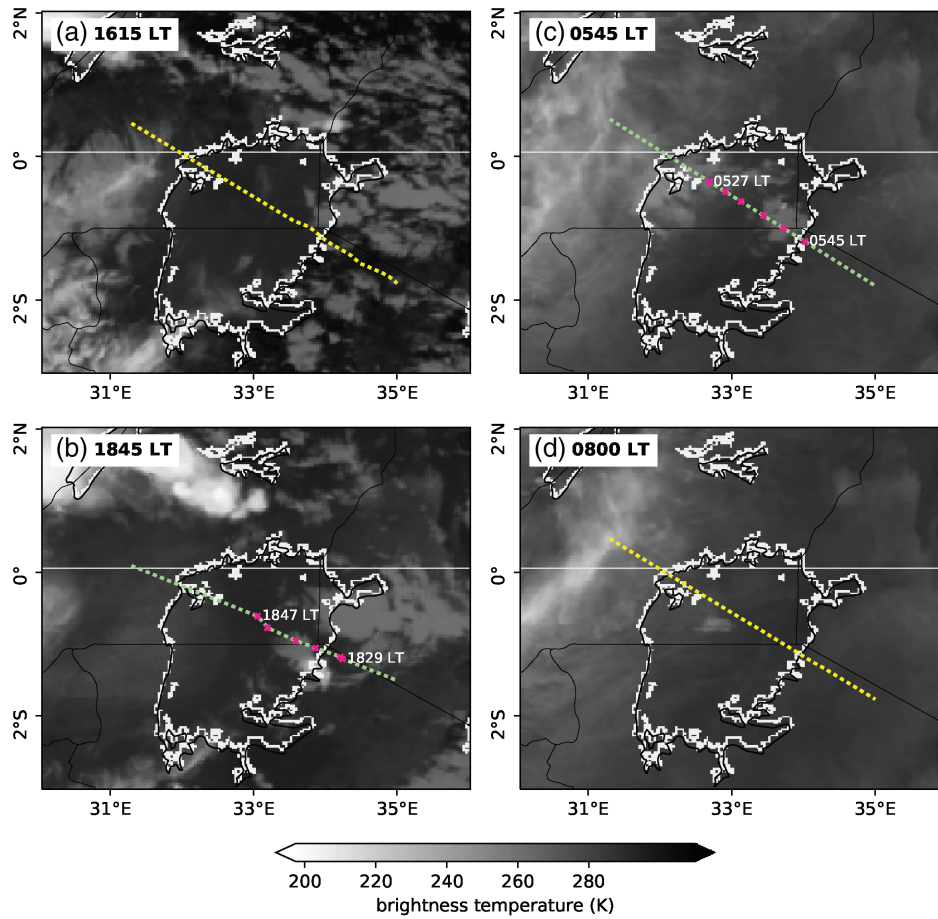


FIGURE 3 METEOSAT 10.8 μm brightness temperature images closest to the times of the sonde drops/runs. Yellow and green dashed lines mark transects along which model cross-sections are computed for flight runs and sonde transects respectively. Pink crosses show where the sondes were dropped, with the time of the first and last drop labelled. (a, b) show the evening flight and (c, d) the morning flight [Colour figure can be viewed at wileyonlinelibrary.com]

amsl over the lake), until turning $180^\circ \sim 75$ km inland and continuing back toward the lake, following the terrain at this height (green–yellow colours). Once over the lake, the aircraft descended to 150 m agl ($\sim 1,300$ m amsl) to complete the return leg. From the sonde drops, an approximate horizontal location and likely depth of a moisture bulge was identified and this was then sampled between 0730 and 0900 LT at various heights between 30 and 500 m agl (1,165–1,635 m amsl, yellow–red colours) and with two aircraft profiles. Aircraft profiles were also performed over the centre of the lake (orange colours), to compare profiles inside and outside the bulge region. Based on W19, the ideal time to search for the bulge feature and sample over-lake convergence would have been around 0200 LT, but restrictions on low-level flying in the dark meant that the near-surface could not have been sampled at this time.

2.2 | Aircraft data

Data were collected using *in situ* instrumentation carried by the FAAM BAe-146 aircraft, described in some detail by Mirza *et al.* (2016). During science sampling, the aircraft maintains an indicated airspeed of 210 knots which, given

the altitude of the lake, results in a typical true airspeed of ~ 120 m·s $^{-1}$ when sampling *in situ*.

Temperature data were collected by a Rosemount Aerospace Inc. Type 102 Non-de-iced Total Temperature Housing fitted with an original open-wire platinum resistance thermometer (PRT) sensing element. Data were recorded at 32 Hz and are reported at 1 Hz. While measurements are susceptible to drift, this type of instrument is expected to have an accuracy better than ± 0.5 K. Humidity was sampled using a combination of a slow-response well-calibrated chilled-mirror hygrometer (Buck Research Instruments CR2 with heated inlet) and a fast response tunable-diode laser hygrometer (SpectraSensors Water Vapour Sensing System-II, WVSS-II). While the WVSS-II is not calibrated, chilled-mirror hygrometers, such as the Buck CR2, are known to suffer from excursions when sharp humidity gradients are crossed. Therefore, the fast-response WVSS-II instrument was first compared to the Buck in known ‘good’ periods – away from large humidity gradients and altitude changes – and showed good agreement. This allowed the WVSS-II to be used to sample the more challenging environments. Data are reported at 1 Hz. A flush-mounted inlet was used to provide the sample to the WVSS-II. The location of the

TABLE 2 Details of nested convection-permitting MetUM model runs

Horizontal grid-spacing	Grid-points	Domain size (km)	Model timestep (s)
4.4 km	600 × 600	~ 2,600 × 2,650	150
1.5 km	1,000 × 1,000	~ 1,490 × 1,490	60
300 m	2,200 × 2,000	~ 660 × 597	15

flush-mounted inlet within the aircraft boundary layer is not expected to compromise the measurements as it has been shown to perform as well as a Rosemount inlet when sampling humidity concentrations $> 1.0 \text{ g}\cdot\text{m}^{-3}$ (Vance *et al.*, 2015), which is significantly lower than any humidity values encountered during this case-study.

Three-dimensional wind components were sampled at 32 Hz using the nose-mounted FAAM Core 5-port turbulence probe (Mirza *et al.*, 2016). Data were combined with position and aircraft altitude information from the Applanac POS AV 410 GPS-aided Inertial Navigation Unit (GIN) system and rotated on to the transect heading to give along-transect wind speeds at 1 Hz. Quality control analysis showed some evidence of a weak heading dependency to wind direction in the data. This is likely related to imperfectly specified calibration coefficients for alignment of GIN components, resulting in rotation errors for the wind vector. Comparison of the rotated along-transect wind speeds with a supplementary turbulence probe located on the wing – the Aventech Research Inc. (non-standard processing) AIMMS-20 (Beswick *et al.*, 2008) – showed good agreement, suggesting that this error is not significant for this study (not shown). Vertical velocity perturbations w' at 32 Hz around the mean value are taken as a proxy for turbulence intensity, since turbulent kinetic energy (TKE) is proportional to w'^2 (Petersen and Renfrew, 2009).

Temperature, pressure and humidity were also measured using Vaisala RD94 dropsondes launched from the aircraft when at high altitude. Data were transmitted to the Vaisala Airborne Vertical Atmospheric Profiling System (AVAPS) receiver on board the aircraft at a frequency of 2 Hz. The fall speed of the sondes varied from ~ 10 to $15 \text{ m}\cdot\text{s}^{-1}$, therefore measurements were taken every $\sim 5\text{--}8 \text{ m}$.

Thermodynamic quantities potential temperature (θ) and virtual potential temperature (θ_v) were computed using inputs of pressure, temperature and specific humidity from the aircraft data and sondes. Virtual potential temperature takes into account the temperature and moisture content of air and can be used as a proxy for buoyancy. It is given by

$$\theta_v = \frac{\theta(w + \epsilon)}{\epsilon(1 + w)},$$

where w is the mixing ratio (approximated by specific humidity) and $\epsilon \approx 0.622$ is the ratio of the gas constant for

dry air to the gas constant for water vapour (Markowski and Richardson, 2010).

2.3 | MetUM simulations

CP MetUM simulations were run for the campaign period. The model simulations are presented as a companion to understand which processes are consistent between observations and model, and how model resolution impacts this. The regional model set-up was the same as that described in W19 – based on the Even Newer Dynamics for General Atmospheric Modelling (ENDGAME) dynamical core (Wood *et al.*, 2014) – except with the new Regional Atmosphere 1 for the Tropics (RA1T; Bush *et al.*, 2019) configuration. Of note is the use of the zero lateral flux (ZLF) scheme of Zerroukat and Shipway (2017), which ensures that mass is conserved and reduces the excessive rainfall rates seen in Woodhams *et al.* (2018). For the boundary layer, a “blended” parametrization scheme (Boutle *et al.*, 2014) was used which, dependent upon the ratio between the model resolution and turbulent length-scale, seamlessly transitions between a 1D vertical turbulent mixing scheme suitable for coarse resolutions (Lock *et al.*, 2000) and a 3D turbulent mixing scheme based on Smagorinsky (1963).

Simulations were triply one-way nested, with horizontal grid-spacings of 4.4, 1.5 km and 300 m (Figure 1 and Table 2); the latter is of far higher resolution than any operational model currently in the region. The 4.4 km nest was driven by boundary conditions from the European Centre for Medium-Range Weather Forecasts (ECMWF) Integrated Forecasting System (IFS) model. The regional model nests had 80 terrain-following vertical levels up to a lid of 38.5 km. The simulations were run out to T+ 60 hr with model data output every hour. Runs initialised at 0000 UTC and 1200 UTC on 25 January 2019 were used to compare to aircraft data from the evening and morning flights respectively.

Foundation water surface temperatures (temperature below the diurnal warm layer) from the Operational Sea Surface Temperature and Sea Ice Analysis (OSTIA) were used for the lake surface temperature (LST) (Fiedler *et al.*, 2014; Good *et al.*, 2020). OSTIA includes satellite sea surface temperature (SST) data from the Group for High Resolution SST (GHRSSST) and *in situ* data received via

the Global Telecommunication System (GTS), although no *in situ* observations are currently reported from Lake Victoria. Fiedler *et al.* (2014) showed that OSTIA LSTs over Lake Victoria have smaller differences from observations than other lakes, possibly due to its equatorial location, large surface area and relatively low elevation. Although Fiedler *et al.* (2014) reported several hundred satellite observations over the lake per day in June–August 2009, the presence of cloud over the lake during storms will reduce the number of useable observations.

For consistency, θ and θ_v were computed in the same way as for the observations (i.e., these variables were not output directly from the model).

2.4 | Satellite observations and analyses

Brightness temperatures were computed from the $10.8\ \mu\text{m}$ IR satellite images produced by the Spinning Enhanced Visible and Infrared Imager (SEVIRI) instrument on board the Meteosat Second Generation Satellite (Schmetz *et al.*, 2002). The digital number in the image was converted to brightness temperature using the relationship in Chamberlain *et al.* (2014, their equations 1 and 2). Rainfall rate observations from the IMERG Final Precipitation version 06 product on a 0.1° grid from the Global Precipitation Measurement (GPM) mission (Huffman *et al.*, 2019a; Huffman *et al.*, 2019b) were used to compute rainfall anomalies for the period. A full description and review of GPM can be found in W19. Analyses from ERA5 (C3S, 2017; Hersbach *et al.*, 2020) on a 0.25° grid with 37 pressure levels and time resolution of 1 hr are used to compare the study period with climatology.

3 | RESULTS

3.1 | Synoptic conditions

Between 14 and 26 January 2019, the Lake Victoria basin (Figure 2a) received almost 50% more rainfall than the 2000–2018 average for that period (based on GPM IMERG, not shown). Note that periods of convection are not unusual in this dry season (Yin and Nicholson, 1998), and this enhancement of rainfall was likely due to an active MJO in phases 3 and 4 (Pohl and Camberlin, 2006a; 2006b; Hogan *et al.*, 2015) between 14 and 21 January, as well as a Kelvin wave passage across the region. By the time of the campaign, the MJO had moved into phase 6, which tends to suppress rainfall activity in the region. However, isolated convective events continued to occur over the lake. In particular, significant storms occurred on the three nights preceding the first flight (not shown).

Over the lake, 10 m winds had a westerly anomaly during the campaign associated with an increased 2 m temperature gradient between the northwest and southeast of the lake (Figure 4c). Relatively warmer air along the eastern shore and to the south of the lake were associated with a northeasterly 10 m wind anomaly over western Kenya and northern Tanzania and increased low-level convergence along the eastern shore. To the east of the lake, air at 850 hPa was up to $2\ \text{g}\cdot\text{kg}^{-1}$ drier than climatology, whereas over the north and west of the lake the air was approximately $1\ \text{g}\cdot\text{kg}^{-1}$ wetter (Figure 4f). At 700 hPa, air was $\sim 1\ \text{g}\cdot\text{kg}^{-1}$ drier than climatology over large parts of the Lake Victoria Basin (Figure 4i). 700 hPa winds were similar to the climatology over the lake, but a northerly anomaly was present to the east and south of the basin. Relatively dry air at 850 and 700 hPa likely explain the lack of deep convection during the campaign period, although overall the conditions are fairly representative for the time of year.

3.2 | Evening flight

Figure 5 shows data along the flight transect at $\sim 300\ \text{m}$ agl between 1550 and 1638 LT during the evening flight (Figure 3a). Figure 6 shows data from the sonde drops in Figure 3b between 1829 and 1847 LT. Output from the 300 m model at 1600 LT (T+37 hr forecast) and 1900 LT (T+40 hr forecast) is plotted underneath the observations in Figures 5e–g and 6 respectively. Figures 5a,b,e,f show that the LBF at $\sim 300\ \text{m}$ agl ($\sim 1740\ \text{m}$ amsl) was observed between 45 and 50 km inland from the eastern shore at approximately 1627 LT (marked by red arrows). The direction of the along-transect wind reversed across the front, changing from approximately $+3\ \text{m}\cdot\text{s}^{-1}$ (westerly) to $-5\ \text{m}\cdot\text{s}^{-1}$ (easterly) over $\sim 5\ \text{km}$. Over the same distance, specific humidity decreased by $\sim 6\ \text{g}\cdot\text{kg}^{-1}$. The specific humidity continued to decrease at a lower rate ahead of the front, in total falling $\sim 9\ \text{g}\cdot\text{kg}^{-1}$ over $\sim 20\ \text{km}$. Profiles from the sonde drops show that the lake breeze was still present over land $\sim 2\ \text{hr}$ later and provide information about the vertical structure of the lake breeze (Figure 6). In both sonde B over land (25 km onshore) and sonde E over the lake (75 km offshore), very moist air ($14\text{--}15\ \text{g}\cdot\text{kg}^{-1}$) and westerly winds were observed over the lowest $\sim 300\ \text{m}$ (Figure 7a–c, black lines). A lake breeze depth of $\sim 300\ \text{m}$ suggests that the 1550–1638 LT transect was taken very close to the top of the lake breeze layer.

During the 300 m agl transect, cumulus congestus were recorded by an observer on the aircraft, close to where the LBF was observed over land. Low clouds just onshore in Tanzania are also visible in the satellite image at 1615 LT (Figure 3a). By 1645 LT, the congestus in the vicinity

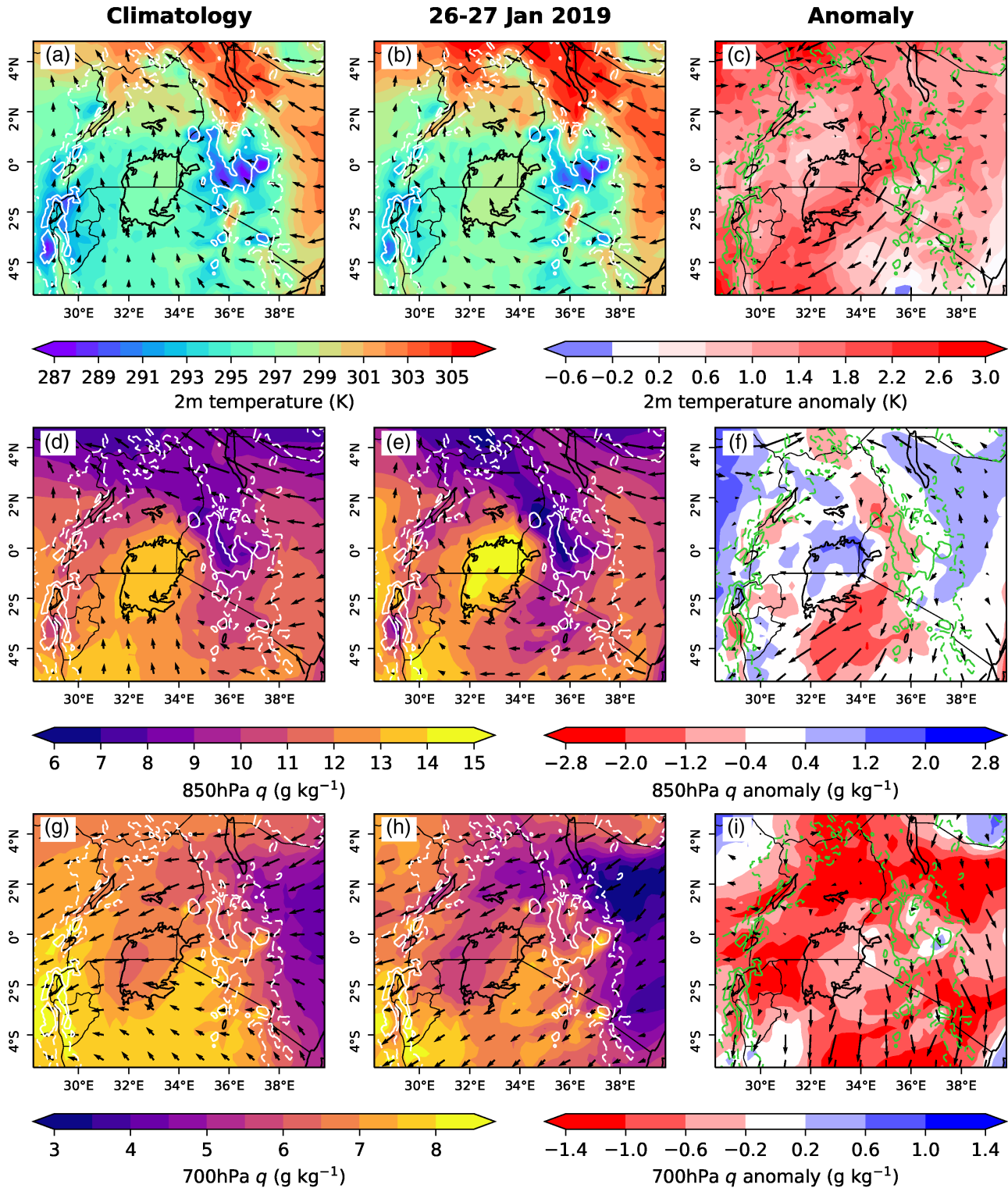


FIGURE 4 Synoptic situation during HyVic flights. (a–c) 2 m temperature (shading) and 10 m winds (arrows), and (d–f) 850 hPa and (g–i) 700 hPa specific humidity (shading) and winds (arrows). (a, d, g) show mean climatology from 1979–2019 for the two-week period surrounding the HyVic flights (19 January–3 February), (b, e, h) show means during the HyVic period (26–27 January 2019) and (c, f, i) show the anomaly from the climatology during the HyVic period. Data from ERA5. White and green dashed (solid) contours show 1 (2) km orography [Colour figure can be viewed at wileyonlinelibrary.com]

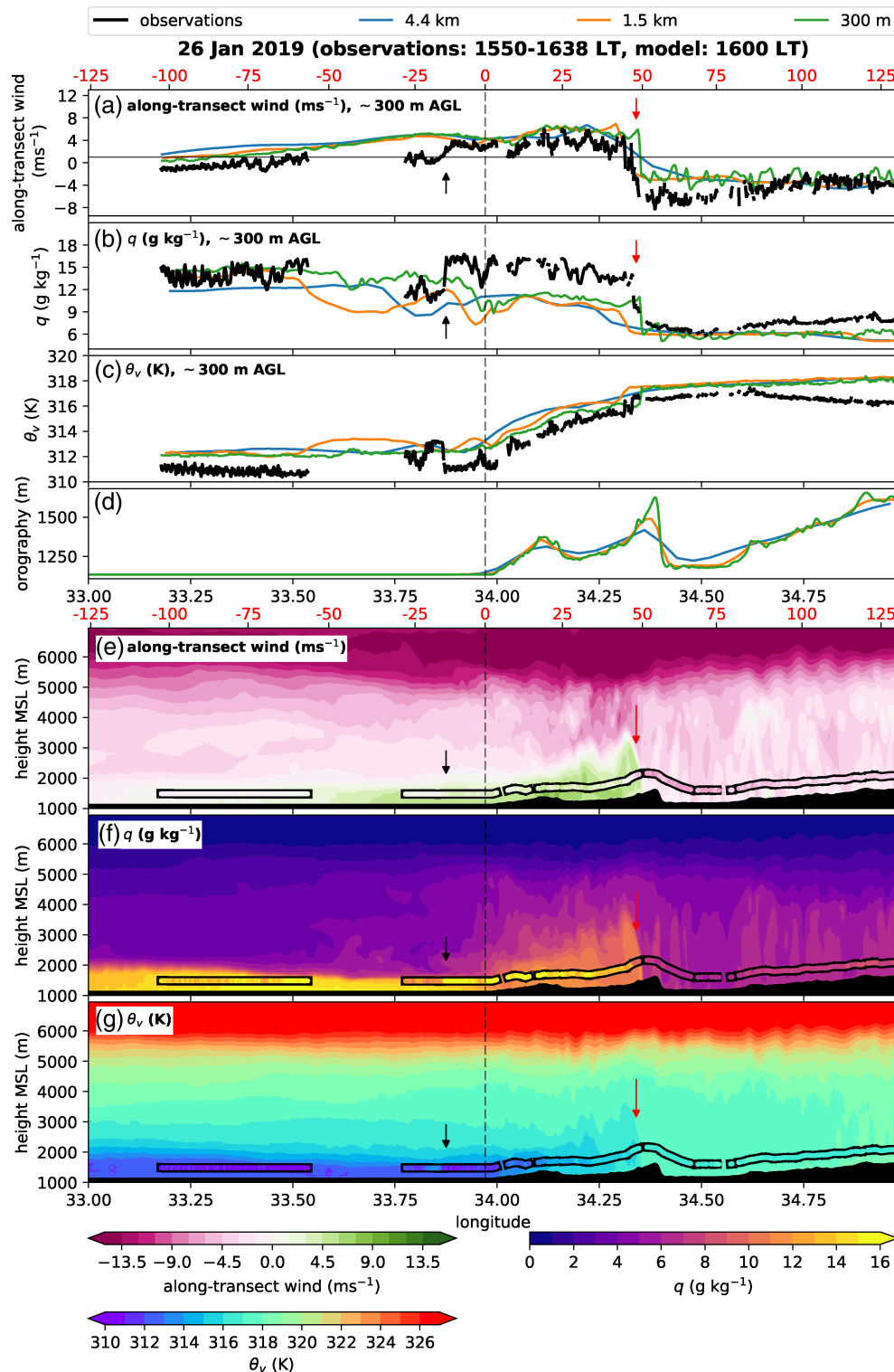
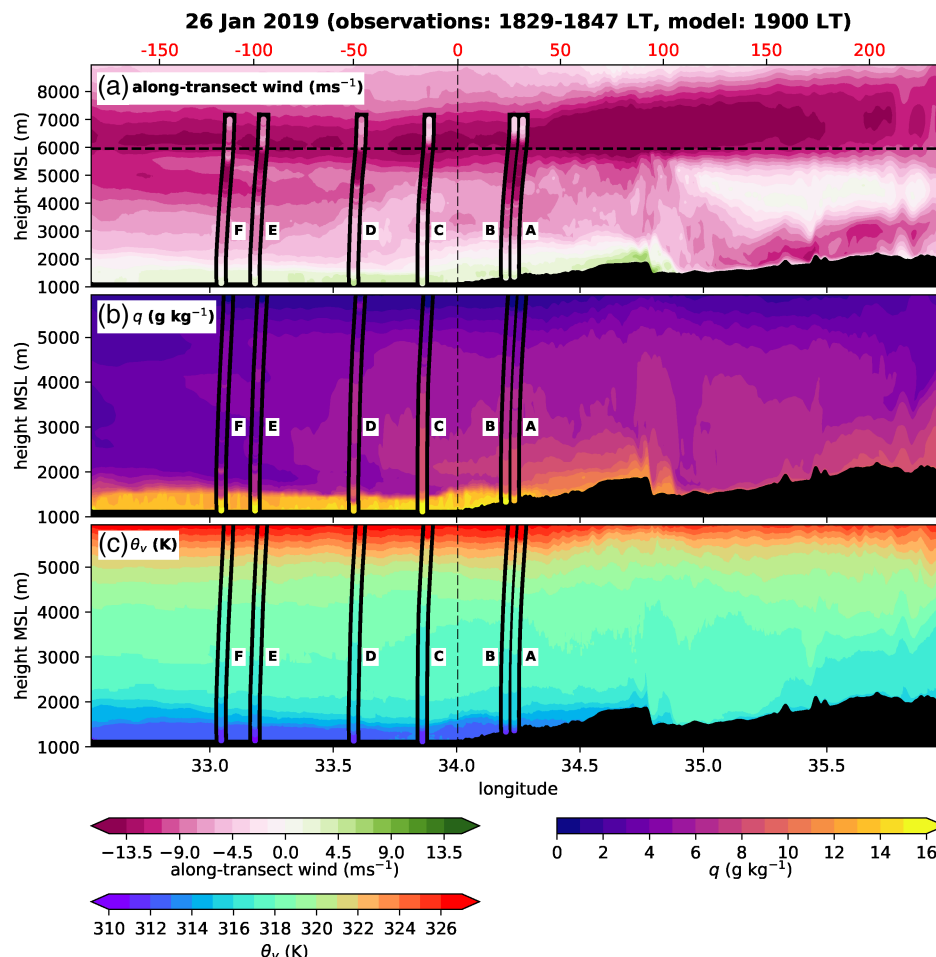


FIGURE 5 Aircraft observations (black) of (a) along-transect wind, (b) specific humidity and (c) virtual potential temperature along a ~ 300 m agl ($\sim 1,400$ m amsl when above the lake) run moving from the lake (northwest) to land (southeast) between 1550 and 1638 LT during the evening flight. Data are missing between 33.55 and 33.77°E where the aircraft had to move off its path to comply with air traffic control. Simulated variables from CP MetUM with three different horizontal grid-spacings are also plotted (colours), obtained from a virtual fly-through of the model along the aircraft track at 1600 LT (T+37 hr forecast). (d) Orography from the three model resolutions. Cross-sections of (e) along-transect wind, (f) specific humidity and (g) virtual potential temperature from the aircraft observations are shown within bold black lines, with simulated variables (from the 300 m model) plotted behind. Aircraft and model data in (e–g) are from the same times as in (a–c). The distance in km from the eastern shore of the lake (black dashed line) are shown in red, with positive (negative) numbers onshore (offshore). The red arrows mark the position of the lake breeze front and the black arrows mark a second front observed offshore [Colour figure can be viewed at wileyonlinelibrary.com]

of the LBF had developed into deep convection, likely triggered by convergence at the front. This convection lasted ~ 1.5 hr, remaining as a small, isolated cumulonimbus before decaying shortly before sunset. Relatively cold cloud is shown close to the flight track in the satellite image at 1845 LT, likely remnants of the observed storm (Figure 3b).

In the sonde profiles, easterlies were observed above the westerly lake breeze flow from 1,500 m amsl (~ 350 m agl) over the lake and 1,750 m amsl (~ 425 m agl) over the land (Figure 7c). The strength of the easterly wind generally increased with height up to ~ 6 km amsl over both the land and lake, above which there was a sharp reduction in along-transect wind. All sondes show a particularly strong

FIGURE 6 Cross-sections of (a) along-transect wind, (b) specific humidity and (c) virtual potential temperature during the evening flight. Dropsonde observations between 1829 and 1847 LT are shown within bold black lines, and the simulated variables from the 300 m model configuration at 1900 LT ($T+40$ hr forecast) are plotted behind. The distance in km from the eastern shore of the lake (black dashed line) are shown in red, with positive (negative) numbers onshore (offshore). Note that the transect extends further west and east than in Figure 5. Also note the different height scale in (a), where the black dashed line shows the maximum height in (b) and (c) [Colour figure can be viewed at wileyonlinelibrary.com]



band of easterlies between 4 and 6 km amsl (Figure 6a). Between 5 and 6 km amsl, moisture decreased to almost zero and potential temperature increased rapidly with height (Figures 7a,b), such that this inversion likely marks the start of the free troposphere. A similar band was simulated by the model (although at 6–8 km amsl) and shown to extend across the whole transect. Air in the mid-level region (below the free troposphere, but above the lake breeze) was fairly well-mixed. It was warmer and drier than the lake breeze layer, but cooler and moister than the air above. This layer of air likely corresponds to the lakeward return flow of the lake breeze (Thiery *et al.*, 2015; W19). The top height of the return flow is unclear due to the strong band of easterlies between 4 and 6 km amsl, which mask the signal.

The return flow can be better visualised from the cross-section plots and simulations. At 1600 LT, the 300 m model shows a region of stronger easterlies between 3 and 5 km amsl (below the band of strongest easterlies between 5 and 7 km amsl at this time) which extend from the leading edge of the lake breeze back to ~ 15 km onshore (Figure 5e). Figure 5f shows enhanced specific humidity in this region, where the return flow advects moisture from the lake breeze – which has been mixed upwards

over land – back toward the lake. At this time, no observations were recorded in this return flow region; in hindsight, the altitude of the mid-level leg designed to sample the return flow (~ 6 km amsl, 1756–1813 LT) was higher than the return flow region identified in the sonde profiles. By 1900 LT, the simulated LBF has moved further onshore ($\sim +110$ km) and the lakeward return flow has extended further back over the lake (Figures 6a,b). The extent of the return flow is less clear in along-transect wind than at 1600 LT, since the prevailing easterly winds have generally strengthened at all heights across the transect. Some of the air in this easterly flow may also have originated from the low-level easterlies ahead of the LBF, having been lifted over the denser lake breeze air. The extended influence of the return flow is clear in the specific humidity, with values >3 g·kg $^{-1}$ extending approximately 175 km offshore (Figure 6b). The lakeward return flow is clearly visible in sondes A and B over land, with strong easterlies and high specific humidity above ~ 2.5 km amsl (Figures 6a,b). Sondes C and D (15 and 35 km offshore respectively) also show enhanced specific humidity up to ~ 4.5 km amsl (6–8 g·kg $^{-1}$ at 3 km amsl, compared to 3.8 g·kg $^{-1}$ in E and F further west over the lake), but the easterlies are reduced compared to A and B (-3 – 5 m·s $^{-1}$

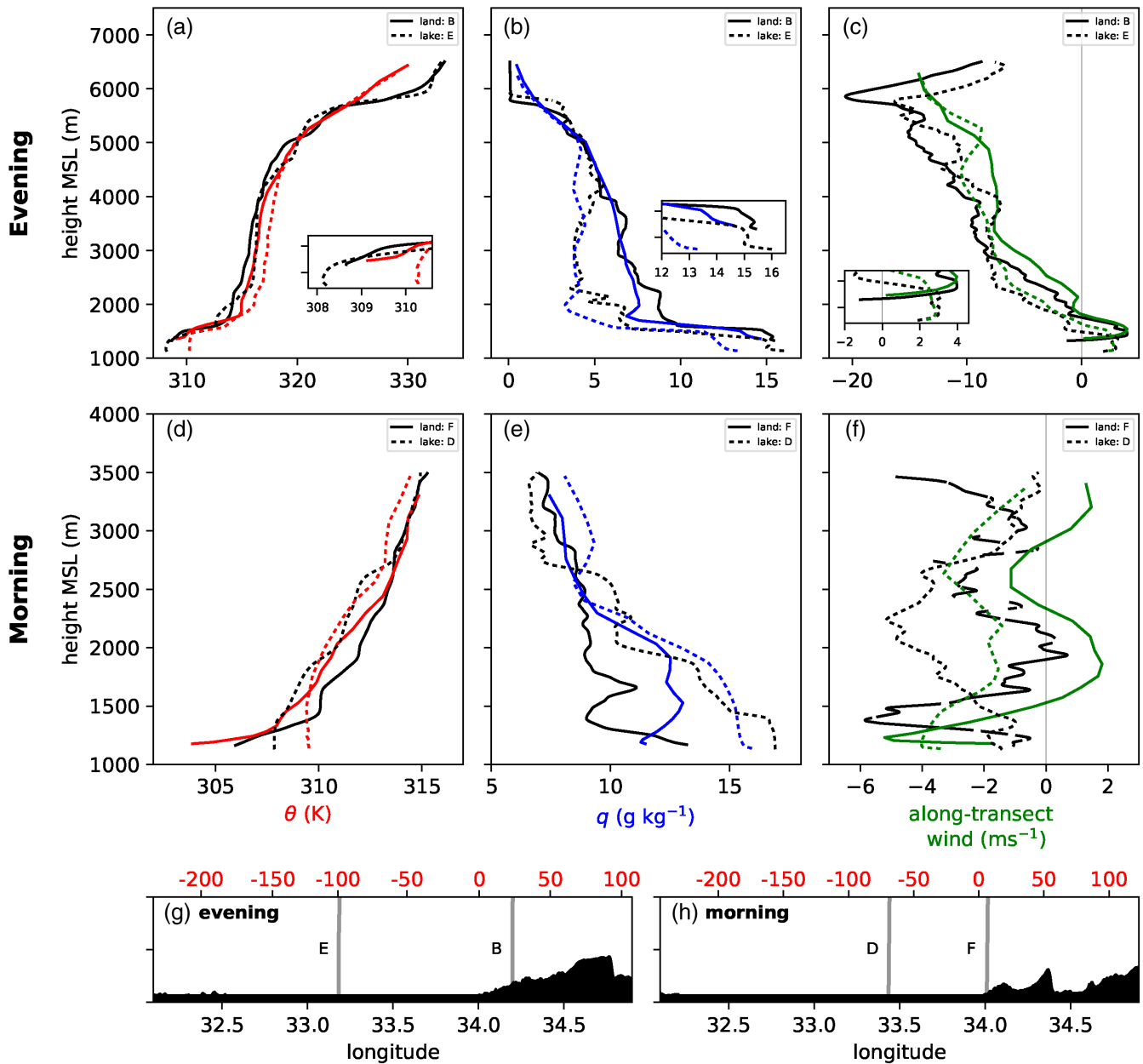


FIGURE 7 Profiles of observed (black, from dropsondes) and simulated (colours, from the 300 m model) (a, d) potential temperature, (b, e) specific humidity, and (c, f) along-transect wind (positive winds approximately correspond to westerlies) during the (a–c) evening and (d–f) morning flights. Dashed lines show profiles over Lake Victoria and solid lines show profiles over land to the east of the lake. Note the different vertical scales in the first and second row of plots. Inset axes in (a–c) show a zoom of the lowest 1,500 m agl. In (g, h) the locations of the sonde drops are shown by the grey lines for (g) the evening and (h) the morning flights. The distance in km from the eastern shore of the lake is given by the red numbers and the letters correspond to the sonde labels in Figures 6 and 8 [Colour figure can be viewed at wileyonlinelibrary.com]

versus similar to -8 ms^{-1}). Sondes E and F both show increased easterlies above 2.5 km amsl (similar to -8 m s^{-1} at 3 km amsl) compared to sondes C and D. The simulation also shows a reduction in the along-transect wind in the region around sondes C and D and an increase around sondes E and F between 3 and 5.5 km amsl. At least in the simulation, the increased easterlies around the locations of sondes E and F are related to downward motion of air from the strong easterly band at 6–8 km amsl, possibly as a

result of divergence over the centre of the lake (not shown). The transect in Figure 6 is extended further to the east than Figure 5 to show the landward branch of the return flow east of the LBF, manifested in reduced easterlies between 3 and 5 km amsl east of +100 km (Figure 6a).

At the surface, cooler air was observed over the lake than over the land by the dropsondes (Figure 7a). Over the lake, potential temperature decreased with height through the lake breeze layer. Over land, the air was stable over

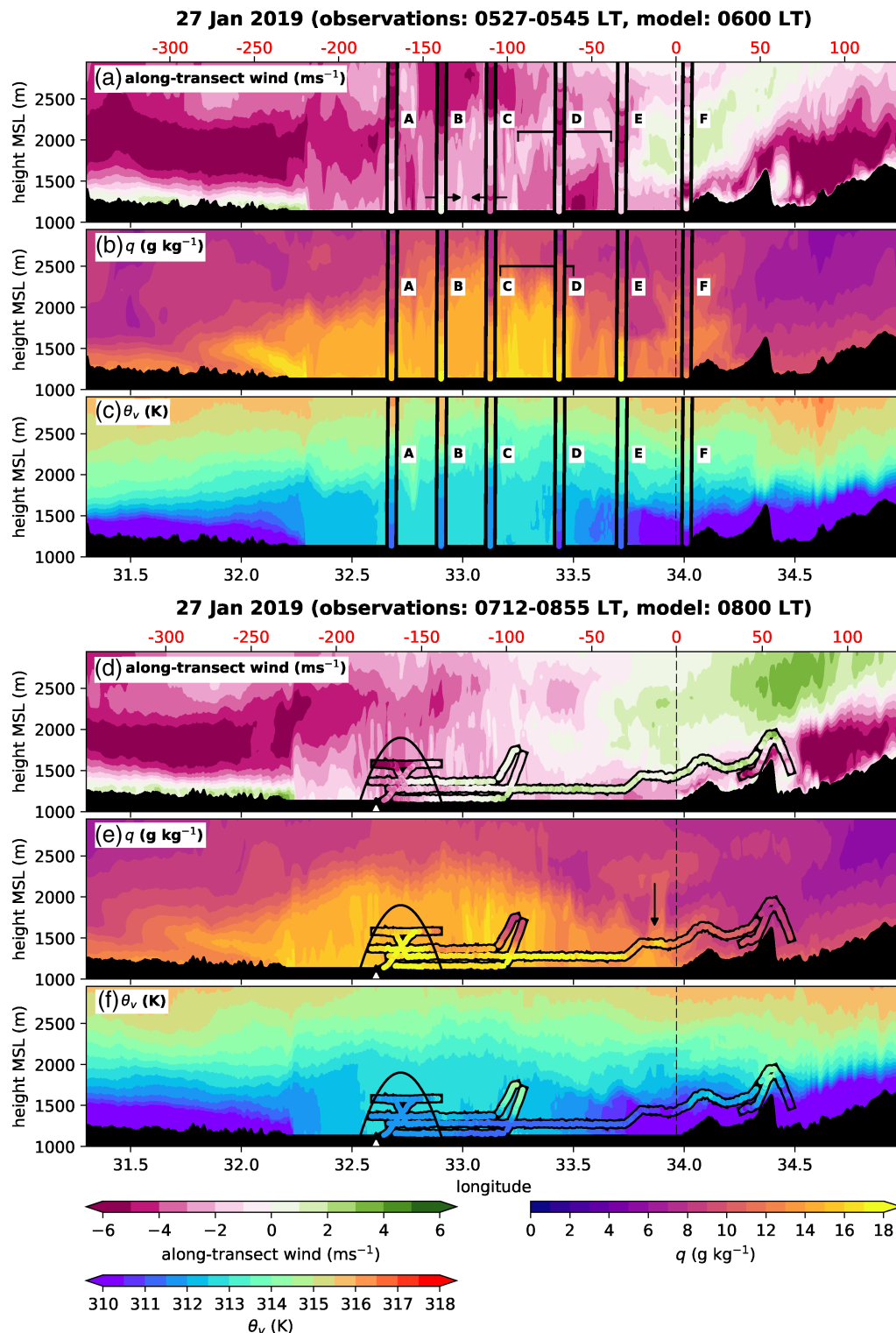


FIGURE 8 Cross-sections of (a, d) along-transect wind, (b, e) specific humidity and (c, f) virtual potential temperature from (a–c) sondes between 0527 and 0545 LT and (d–f) the aircraft between 0712 and 0855 LT during the morning flight are plotted within bold black lines. The simulated variables from the 300 m configuration from (a–c) 0600 LT (T+39 hr forecast) and (d–f) 0800 LT (T+41 hr forecast) are plotted behind the observations. All plots share the same x-axis (longitude) but the distance in km from the eastern shore of the lake (red numbers) differ between (a–c) and (d–f) due to slightly different flight tracks. The black arrows in (a) show convergence between sondes B and C. The black bracket in (a, b) shows the detached land-breeze front. The parabola in (d–f) shows the approximate location of the bulge feature. The arrow in (e) shows the location of a second potential moisture bulge near the eastern shoreline. The white triangle in (d–f) shows the location of the Ssesse Islands [Colour figure can be viewed at wileyonlinelibrary.com]

the lake breeze layer, suggesting that the cooler air moving from the lake to the land had a stabilising effect at the surface. Above the lake breeze, there was an inversion and drying (Figures 7a,b). An interesting feature in the land profile was the distinct layer of well-mixed air between $\sim 1,500$ and $2,200$ m amsl (~ 350 – $1,050$ m agl) just above the inversion. This layer was cooler and moister than the air above. There is also evidence of this well-mixed layer between $1,600$ and $2,000$ m amsl (~ 350 – 950 m agl) in sonde E over the lake (black dashed lines). This layer could have been a remnant of the lake boundary layer from the previous morning.

An unexpected feature was observed during the 300 m agl transect. Approximately 15 km offshore ($\sim 33.88^\circ\text{E}$, indicated by black arrows in Figure 5), the aircraft observations show another sharp front in both wind and moisture. In the direction of the shoreline, specific humidity increased by ~ 5 g·kg $^{-1}$, and the wind increased from nearly stagnant to $\sim +4$ m·s $^{-1}$ (westerly). The cause of this front over the lake remains unclear, especially because of the missing data to the west. The transition was too far behind the LBF to be attributed to the aircraft passing into a head region of the flow and, since the transition occurred offshore, it cannot be related to the deepening of the lake breeze by the convective boundary layer over land. Deepening of the lake breeze just offshore may occur if air is decelerated at lower levels by increased surface friction (as the flow moves onshore), or if the flow is blocked by orography, causing it to stagnate and force incoming air upwards (e.g., Jiang, 2003; Hughes *et al.*, 2009). However, the vertical velocity observed by the aircraft does not show any changes across this transition (not shown). Given that the depth of the lake breeze layer was approximately 300 m (Figure 6), one explanation may be that on the 300 m agl leg, the aircraft was located just above the lake breeze layer to the west of 33.88°E and moved inside the breeze east of this point. This hypothesis is supported by the neutral/easterly winds to the west of 33.88°E .

3.3 | Morning flight

During the morning flight, sonde drops were used to identify signals of a land breeze across the eastern shore and the location of a potential moisture bulge similar to that in W19. The aircraft then sampled the identified bulge region at various heights, providing further insight into the formation and characteristics of the bulge.

The along-transect winds, specific humidity and virtual potential temperature θ_v measured from the sonde curtain (between 0527 and 0545 LT) are shown in Figures 8a–c. Output from the 300 m model at 0600 LT (T+39 hr forecast) is plotted behind the observations for

comparison. One sonde (F) was dropped over land, very close to the eastern shoreline. Strong easterly winds between 1,300 and 1,500 m amsl (150–350 m agl), and low θ_v in the lowest 200 m agl, indicate a shallow land breeze across the eastern shoreline. Compared to the sondes over the lake, sonde F is much drier at the surface, and particularly dry in the band of strongest land breeze winds (Figures 8a,b).

Moving westward across the lake, sondes E and D also show weak easterlies close to the surface, but no signal of the strong band of easterlies close to the surface in sonde F. Sonde C (~ 110 km from the eastern shore) shows an increase in near-surface easterlies compared to D and E, whereas sonde B (~ 25 km west of C and ~ 90 km east of the western shore) shows weak westerlies over the lowest ~ 100 m. It is unlikely that these westerlies were related to a land breeze across the western shore since sonde A shows low-level easterlies and the simulation suggests that the LBF would only be located ~ 10 km offshore at this time. The change of wind direction between sondes B and C indicates low-level convergence in this region (horizontal arrows in Figure 8a). The greater and deeper moisture in sonde B (specific humidity of 10 g·kg $^{-1}$ as high as 2,370 m amsl compared to 2,100 m amsl in sonde C) supports the suggestion of convergence as it indicates near-surface moist air lifted by the resulting vertical motion (Figure 8b).

The model simulations (all configurations) provide insight into the observations; at 2200 LT on the previous evening, the simulations show the formation of a weak land breeze (~ 1 m·s $^{-1}$ at the surface) over the lowest ~ 100 m across the eastern shore (not shown). The land breeze strengthens and deepens to ~ 500 m agl through the night, in part as the prevailing easterlies strengthen and katabatic winds likely form. Just offshore, moisture from close to the lake surface is lifted upward into a bulge feature as the land breeze collides with the warmer air over the lake, similar to the formation of the bulge in W19. At 0400 LT, the head region of the land breeze separates from the easterly flow behind and independently propagates westward across the lake, along with the lofted moisture. In its wake, the winds remain easterly, but are weaker, indicating divergence behind the propagating feature. In the simulations, this process occurs across the whole length of the lake, mainly parallel to the eastern shore, but turning to be parallel to the southern shore at the south end of the lake (not shown). The black brackets in Figures 8a,b mark the position of the detached front of the simulated land breeze between 33.25 and 33.7°E at 0600 LT, with the moisture bulge feature slightly ahead between 33.2 and 33.5°E . If a similar process occurred in reality, the deeper moisture in sonde B and strong easterlies in sonde C suggest that sonde C was located within the propagating detached LBF, whereas sonde B was located within the deeper moisture

ahead. If present, this feature was located further west in the observations than in the simulations, suggesting either that it was propagating at a greater speed, or that it formed earlier in the night. Assuming that the observed bulge feature was propagating westward, divergence to its east (weakening easterlies from west to east) may indicate that it had wave-like properties, since divergence could be associated with a trough behind the peak. Although not indicated by the simulations, the low-level westerlies in sonde B could also be a detached land breeze head from across the western shore.

Figures 8d–f show aircraft observations from low-level flying between approximately 0700 and 0900 LT, with corresponding data from the model plotted for 0800 LT (T+41 hr forecast). Along the transect ~ 300 m agl (~ 1450 m amsl), two regions of increased specific humidity – possible bulge features – were located at $\sim 33.9^\circ\text{E}$ (under arrow in Figure 8e) and $\sim 32.75^\circ\text{E}$ (under parabola in Figures 8d–f), where measurements exceeding $17\text{ g}\cdot\text{kg}^{-1}$ were taken. For comparison, specific humidity at this height during the evening flight was between 6.6 and $9.6\text{ g}\cdot\text{kg}^{-1}$ and values exceeding $15\text{ g}\cdot\text{kg}^{-1}$ were not recorded above 30 m agl. These regions of high water content approximately correspond to locations where clouds were observed along a $\sim 1,000$ m agl leg flown between 0650 and 0710 LT (with some differences due to the time delay between the various legs). Around 0530 LT, Figure 3c also shows two regions of low cloud over the lake (one to the west and one to the east) corresponding to the observed locations.

Given the time constraints of the flight, the eastern bulge was sampled at just one height. The western bulge was chosen to be sampled in detail because it was close to the region of increased moisture depth identified in the sondes (sonde B, $\sim 32.9^\circ\text{E}$) and because the bulge would be expected over the western half of the lake at this time (W19, their figures 7j–l and 14d–f). Between 32.6 and 32.9°E , the boundary layer was sampled at four heights (between ~ 30 and 500 m agl) and along two profiles. Around 32.8°E , specific humidity exceeding $17\text{ g}\cdot\text{kg}^{-1}$ extended to a depth of at least 440 m agl ($\sim 1,650$ m amsl). At the same height at 33.25°E (~ 60 km east of the bulge), specific humidity of only 8 – $10\text{ g}\cdot\text{kg}^{-1}$ was recorded. Along the transect, the horizontal extent of the high moisture decreased with height, implying a dome shape (suggested by the parabola in Figure 8e). The location of the deepest moisture compared to that observed in sonde B confirms westward propagation of the feature of 10 – 20 km in 2 – 3 hr. During these runs, the observed along-transect winds remained easterly within the bulge region, with a switch to westerly winds to the east, suggesting an increase in divergence behind the bulge feature since the sonde drops 2 hr prior. In the simulation, the westward-propagating

region of enhanced easterlies is weakened and no longer visible by 0800 LT, but the deeper moist air remains, located around 33.1°E (having propagated 10 – 20 km westward in 2 hr). Unlike the observations, the simulated winds remain easterly behind the bulge.

Figure 9 shows measurements of the specific humidity, vertical velocity perturbation w' (a proxy for turbulent kinetic energy) and along-transect wind sampled along the transect at different heights within and to the east of the bulge region. The inset axes (numbered) are centred vertically at the mean altitude of each aircraft run and extend horizontally for the length of the run such that all inset axes share the same x -axis (longitude). Data are only shown along straight level runs. The bulge was identified by a sharp increase in specific humidity close to 32.9°E for the three transects below $1,500$ m amsl (inset axes 2–4). Regions inside the bulge are marked by a solid line and regions immediately outside the bulge are marked by a dashed line. A visual inspection of the data suggests that w' was more variable inside the bulge than outside (Figure 9b). The standard deviation of w' confirms this, showing higher variance inside the bulge at all heights (Table 3), although more sampling inside and outside the bulge is required to test the robustness of this difference. The most noteworthy difference in standard deviation of w' occurred at $1,365$ m amsl (~ 230 m agl, inset axis 6), where the standard deviation outside the bulge was less than half that inside the bulge (0.12 versus $0.26\text{ m}\cdot\text{s}^{-1}$). The standard deviation of w' outside the bulge at this height was also approximately two times lower than the samples both inside and outside the bulge along the two lower transects. The similar thermodynamic and TKE characteristics of the air inside the bulge compared to the air at lower altitudes strongly supports the hypothesis that the boundary layer was the source of the air which formed the bulge. The presence of this region of boundary layer air next to a region of quiescent air – likely free-tropospheric air – at 230 m agl suggests that the the boundary-layer air was lifted upward by a process other than normal overturning, likely convergence at low levels. Given the high specific humidity and standard deviation of w' along the highest transect ($1,577$ m amsl, ~ 440 m agl), the aircraft likely only sampled the bulge region at this height and did not fly far enough east to sample air outside the bulge.

In the simulation, a second region of deepened moisture occurs around 32.5°E (Figure 8e), to the west of where the flight transect passed over a section of the Sses Islands (small notch of orography indicated by white triangle at 32.6°E in Figures 8d–f). In the simulation, convergence occurs just to the east of the islands (Figure 8d), likely responsible for the uplift of moist air. The observed bulge was located just to the east of the islands and the aircraft did not sample to the west of the islands.

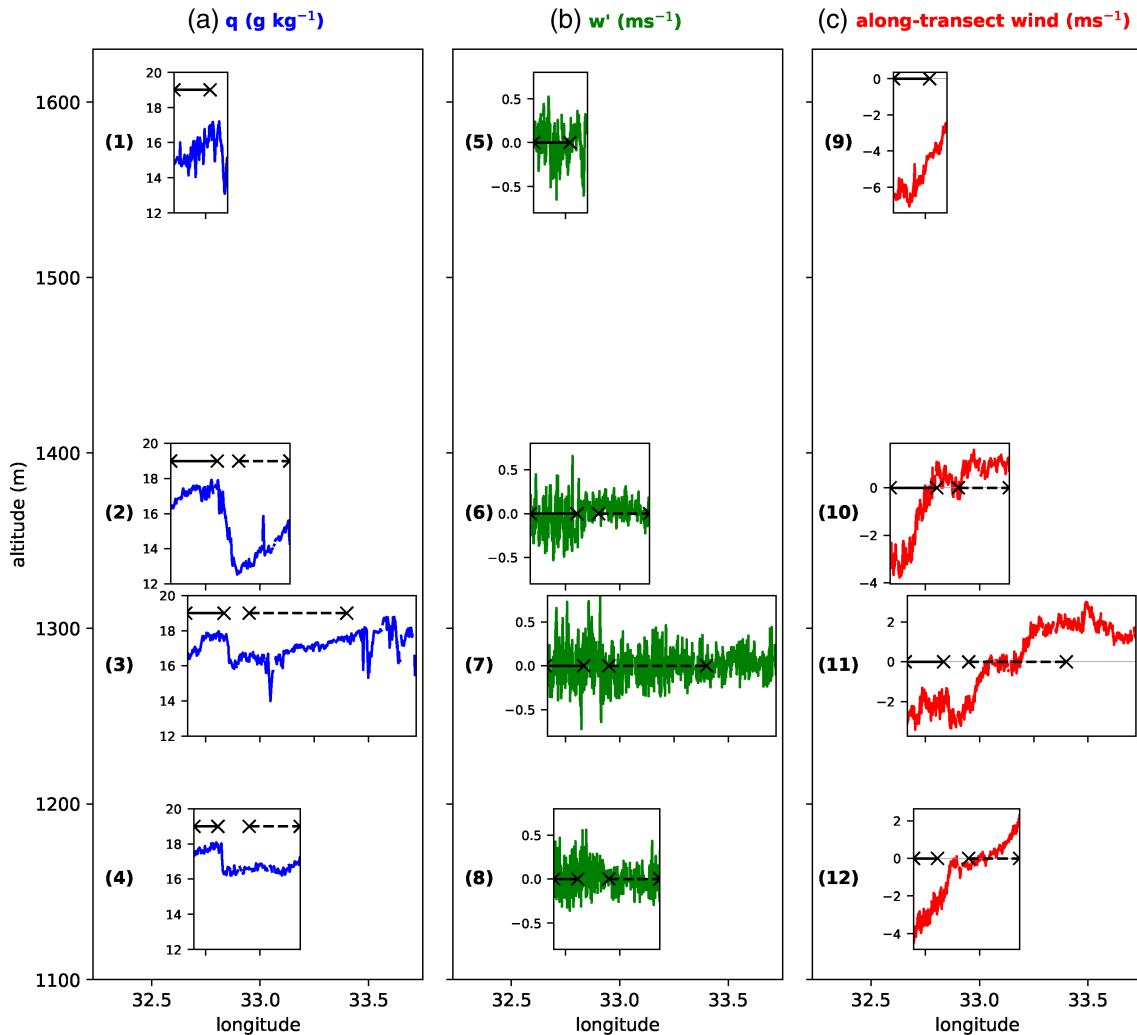


FIGURE 9 (a) Specific humidity q , (b) vertical velocity perturbation w' and (c) along-transect wind over the lake observed between 0733 and 0855 LT during the morning flight. The inset axes are centred vertically on the main axes at the mean altitude of each aircraft run, and extend horizontally for the length of the run such that all inset axes share the same x -axis (longitude). The regions marked by the solid (dashed) black lines in the inset axes of (a–c) show the regions inside (outside) the bulge in Figures 8(d–f) [Colour figure can be viewed at wileyonlinelibrary.com]

TABLE 3 Standard deviation σ of vertical velocity perturbation w' inside and outside the bulge regions marked by the solid and dashed lines respectively in Figure 9

Height amsl (m)	Subplot	σ inside bulge ($\text{m}\cdot\text{s}^{-1}$)	σ outside bulge ($\text{m}\cdot\text{s}^{-1}$)
1,157	8	0.26	0.19
1,279	7	0.29	0.21
1,365	6	0.26	0.12
1,577	5	0.23	

Note: The subplot refers to the numbered inset axes in Figure 9.

It cannot be said whether the easterlies observed inside the bulge were related to the dynamics of the bulge, an effect of the presence of the islands, or a combination of both.

3.4 | Model evaluation

For the prediction of the location and timing of the LBF, the simulations – especially the 300 m configuration – show broad agreement with the observations, which is impressive given the lack of observations available to initialise the model in this region. At the closest model output time (1600 LT, T+37 hr forecast), the LBF is situated in a broadly similar location to the observations for all three model configurations (Figures 5a–c). The location of the front in the 300 m simulation is ~ 3 km further inland than the observations. However, the model snapshot is from approximately 30 min before the aircraft crossed the front at 1627 LT, suggesting that the simulated LBF should be behind the observed front at this time. Therefore, either the rate of inland propagation of the front is too high, or the lake breeze was initiated too early in the simulation.

The lake–land gradient in θ_v at 1600 LT is greater in observations than in the model over the first 75 km onshore (Figures 5c,g), suggesting that the LBF should be ahead in the observations since a stronger θ_v gradient would drive a stronger onshore flow further inland. However, relative to the simulations, stronger observed easterly winds in the 50 km ahead of the LBF (Figures 5a,e; +50 to +100 km), likely offered greater opposition to the propagating lake breeze (Estoque, 1962; Simpson *et al.*, 1977; Arritt, 1993). The stronger observed winds are likely a result of decreasing θ_v ahead of the LBF, compared to a small increase in θ_v in the simulation (Figures 5c,g).

All three model configurations capture the wind reversal and moisture decrease across the front, but the rate of change is too low in the 1.5 and 4.4 km configurations, especially the latter which shows a more gradual change over ~ 30 km. The rate of change across the front in the 300 m simulation is too high, corresponding to a reduced horizontal extent of the front compared to observations. The magnitude of change in along-transect wind is too small in all model configurations because the easterly winds ahead of the LBF are too weak (discussed above). The magnitude of the change in specific humidity is also too small because the air inside the lake breeze is too dry.

All model configurations are able to simulate the return flow above the land breeze, although the level of the free troposphere is 2 km higher in the model. For comparison with observations, sonde F (~ 120 km west of eastern shoreline) recorded specific humidity of $3.8 \text{ g}\cdot\text{kg}^{-1}$ and an along-transect wind speed of $-8.2 \text{ m}\cdot\text{s}^{-1}$ at 3 km amsl, compared to $3.5 \text{ g}\cdot\text{kg}^{-1}$ and $-6.0 \text{ m}\cdot\text{s}^{-1}$ at the same position in the model (Figures 6a,b). In the 1.5 and 4.4 km configurations, the influence of the return flow on specific humidity extends ~ 70 km further west than the 300 m configuration.

Differences in the location, gradient and height of the orography in the model may be responsible for some differences between the location and timing of the LBF between model resolutions and the observations. In particular, the gradient of the orography will affect the strength of anabatic winds which can reinforce the lake breeze. Figure 5d shows how the orographic peak approximately 50 km inland is over 200 m higher in the 300 m configuration than in the 4.4 km configuration, and occurs ~ 5 km further inland.

In general, the depth of the lake breeze at 1900 LT is ~ 100 – 200 m greater in the models than in the dropsonde profiles over both lake and land (Figures 6a,b and 7a–c). Specific humidity within the lake breeze layer is lower in the model than observations (Figure 7b), despite the model being warmer (Figure 7a). Over land, the total amount of precipitable water between the surface and top of the inversion is greater in the model (4.64 versus 3.87 mm) which,

given its greater vertical extent and lower specific humidity, implies that the simulated lake breeze is too dilute. Over the lake, the simulated specific humidity is too low *and* the layer is too dry overall with 4.96 mm of precipitable water between the surface and the top of the inversion in the model compared to 5.65 mm in observations. The model is warmer and drier than observed immediately above the lake breeze layer ($\sim 1,600$ – $2,200$ m amsl) since it does not capture the shallow well-mixed layer at this height (Figure 7a,b).

During the morning flight, the depth of the simulated moisture over the lake extends to a greater depth than in the observations (Figures 7e and 8b). The surface mixed layer is deeper, but more dilute in the model, similar to the bias seen during the morning flight. The mixed layer over the lake is also ~ 2 K warmer in the model at the location of sonde D (Figure 7d). Over land (sonde F), the model is ~ 2 K cooler and more stable than the observations at the surface. The increased density gradient due to the cooler air above land and warmer air over the lake in the observations relative to the model could explain the greater westward propagation of the bulge feature in the observations. While observed specific humidity over land generally decreases with height above the surface, the model shows high water content up to 400 m agl (Figure 7e). The height of the peak land breeze winds are ~ 150 m lower in the model than in the observations (Figure 7f), which could be related to the temperature differences or the representation of orography.

4 | DISCUSSION AND CONCLUSIONS

During late January 2019, the HyVic pilot flight campaign successfully carried out two flights using the FAAM BAe-146 aircraft to sample the lake–land breeze circulation over Lake Victoria in East Africa. An evening and morning flight observed the lake and land breeze circulations at their respective times in the diurnal cycle in unprecedented detail. Notably, this campaign provides the first observations of the vertical structure of the lake–land breeze circulation of Lake Victoria. The observational period was generally dry, allowing the underlying lake–land breeze circulation to be observed without the complicating impacts of storm circulations. High-resolution CP MetUM simulations were run for the campaign period. Model evaluation was performed and, where appropriate, the simulations were used to fill gaps in the aircraft data. This novel observational dataset provides the first detailed measurements of the lake breeze across the eastern shore of Lake Victoria, including the lake breeze front (LBF) and the return flow above. Signals

of a nocturnal land breeze across the eastern shore and its return flow were also identified. The data provides first observational evidence for a moisture bulge – a region of higher and deeper moisture above the lake surface, associated with nocturnal low-level convergence – and insight into the formation and propagation of this feature, which had previously been seen only in simulations by Woodhams *et al.* (2019).

During the evening flight, the aircraft sampled the lake breeze across the eastern shore at a height of ~ 300 m agl, traversing the LBF at 1627 LT approximately 50 km onshore. The inland propagation distance is within that expected from previous literature (references in Section 1), but the maximum extent of the inland propagation is unknown and would require greater spatial coverage of instruments to deduce. The LBF exhibited a wind reversal from westerly to easterly, in which the velocity changed by $\sim 8 \text{ m}\cdot\text{s}^{-1}$, accompanied by a decrease in specific humidity of $6 \text{ g}\cdot\text{kg}^{-1}$ over just 5 km. The width of this LBF is similar to that observed for the Great Salt Lake in the northern USA (Zumpfe and Horel, 2007). Dropsonde profiles between 1829 and 1843 LT showed the depth of the lake breeze layer to be ~ 300 m, in line with studies elsewhere in the world (references in Section 1) although on the lower end. A return breeze layer between 2 and 5 km amsl (1–4 km agl) was identified in the dropsonde profiles, showing that moist air – likely advected over land by the lake breeze – had been transported back toward the lake at mid-levels, extending at least 50 km offshore. A small isolated cumulonimbus was observed to form around 1700 LT in the region of the LBF, with an estimated life cycle of 1.5 hr.

During the morning flight, a land breeze with a depth of 350 m was observed in a dropsonde profile close to the eastern shore at 0545 LT. Land breezes tend to be weaker and shallower than their lake counterparts (Mak and Walsh, 1976), suggesting that the lake breeze observed during the evening flight may have been decaying by the time the dropsonde profiles were taken. The easterly land breeze signal in the dropsonde profiles from the morning flight initially weakened moving offshore, but a region of enhanced easterlies was observed near the centre of the lake (33.1°E , sonde C). Consistent with the accompanying model simulation, it was suggested that the leading edge of the land breeze, indicated by strong easterlies, separated from the main land breeze and independently propagated westward across the lake. At the same time, a region of deeper moisture was identified in the sonde B profile at 32.9°E , just west of sonde C. Sonde B also recorded weak westerlies at the surface, indicating the presence of low-level convergence at the leading edge of the detached land breeze. This convergence was likely responsible for the deeper moisture in sonde B as a result of the uplift of

moist near-surface air, as was the case for the bulge identified in W19. Between 0700 and 0900 LT, a significant region of increased and deeper moisture was sampled by the aircraft between 32.6 and 32.9°E and at various heights between 30 and 500 m agl and along two profiles. This region is very likely to be the same as that identified during the sonde drops, with 10–20 km westward propagation in 2–3 hr. Along the aircraft track, specific humidity exceeding $17 \text{ g}\cdot\text{kg}^{-1}$ was observed to a depth of at least 440 m agl at 32.8°E , compared to 8 – $10 \text{ g}\cdot\text{kg}^{-1}$ at the same height 60 km to the east. Using w' as a proxy for turbulence, it was shown that the bulge was likely formed of boundary-layer air which had been lifted upward by low-level convergence, rather than by normal overturning in the boundary layer.

To the east of the bulge feature, westerly winds were observed at all sampled levels (as low as 30 m agl), indicating an increase in divergence since the sonde drop period approximately 2 hr prior. The westward propagation of a region of deeper and greater moisture – initially formed by convergence related to a land breeze across the eastern shore – is consistent with the bulge feature from simulations in W19. However, in W19, strong easterlies persist behind the bulge as it propagates; there is no detachment of the leading edge of the land breeze nor divergence as observed and simulated during HyVic. While divergence across the lake occurs between 2 and 3 km amsl in the W19 simulation, this is related to a return flow above the low-level convergence (their figure 7f). Given that divergence was observed at just 30 m agl during the flight (Figure 8d), it is highly unlikely that the aircraft was sampling a return flow at this height. The westward propagation of the bulge feature with divergence in its wake suggests that the feature exhibits wave-like characteristics. As far as the authors are aware, a feature like this has not previously been observed or simulated.

The convection-permitting configuration of the MetUM, run with three different horizontal grid-spacings (4.4, 1.5 km and 300 m), was able to reproduce the location and timing of key features and processes with reasonable accuracy, which is a major achievement given the lack of observations assimilated in this region. The location and timing of the LBF were accurate to within ~ 10 km and ~ 30 min. However, the width of the LBF was too great in the 4.4 and 1.5 km configurations and too narrow in the 300 m model. Such a result is unsurprising given that only features with a horizontal extent greater than seven times the horizontal grid-spacing can be properly resolved in a model (Milton *et al.*, 2017), but raises important questions as to how well a 4.4 km configuration – the configuration of the current operational CP MetUM model over tropical Africa run by the UK Met Office – could ever capture the lake–land breeze dynamics. This result may also be compared to Dehghan *et al.* (2018) who suggested

that issues with the representation of diffusion reduced the sharpness of the LBF simulated in their model configurations over Southern Ontario. During the morning flight, all model configurations were able to simulate the wave-like characteristics of the westward-propagating bulge feature. Unsurprisingly, there were differences in the location of the LBF and bulge feature between the model and observations. In both the morning and evening flights, it is unclear whether discrepancies in the locations of fronts and other features were related to differences in the timing of events or propagation speeds. Differences between model configurations and observations may also be related to differences in the representation of orography. Studies such as Roebber and Gehring (2000), Kehler *et al.* (2016) and Dehghan *et al.* (2018) have evaluated the ability of various numerical models to accurately represent and predict lake breeze events. Similar to the present study, they showed increased skill for higher-resolution models. These studies also showed that errors associated with sensitivity to lake surface temperature and prevailing background flow can affect the inland propagation of the breeze. While differences in θ_v gradients and prevailing winds do appear to explain some differences between the model and observations during the HyVic campaign, the spatial coverage of observations is insufficient to fully explain the differences.

In all model configurations, the depth of the simulated lake breeze over land was too great, with warming and dilution of the moisture in this layer. On the other hand, the land breeze depth just inland was too shallow during the morning flight, although also too dry at the surface compared to the observations. Over land, the lowest few hundred metres of the atmosphere were stable during both flights. It is known that stably stratified boundary layers are difficult to simulate in numerical models, related to the parametrization of turbulent diffusion (e.g., Fiedler *et al.*, 2013; Holtslag *et al.*, 2013; Sandu *et al.*, 2013), but further analysis is required to fully address the issue, in particular why the model exhibited different biases between the day and night. Over the lake, the lowest layer of the atmosphere was well-mixed during both flights, but this layer was too warm, dry and deep in the model. Further observations (e.g., surface and top of boundary-layer fluxes) and detailed model simulations are required to understand the origin of the excessive heating and drying in the model.

Although it is difficult to draw robust conclusions from just two flights, the HyVic pilot flight campaign has provided direction and motivation for a future extended aircraft campaign over the region, demonstrating proof of concept that key processes can be observed. Such a campaign should include increased sampling near the surface and a higher density of sonde drops. An aircraft can

sample at many levels, but the atmosphere may quickly evolve between different legs, which makes it difficult to attribute differences to time or location. Accordingly, ground observations – including automatic weather stations, wind profilers, Doppler lidars and radiometers – are required in conjunction with the aircraft. Upper-air observations from radiosondes would be an ideal addition to monitor the atmosphere in the long term. Unfortunately, no radiosonde launches were made from Entebbe during the campaign, but increased reliability of radiosonde launches in the region should be a priority. While basing the flights along a single transect allows the upper levels to be linked to the surface, one shortcoming is that the information recorded is only 2D. In particular, convergence can only be identified along the line of the transect. An ideal tool – both for scientific study and operational forecasting – would be radar, which can complete a 3D scan within a relatively small time window. With radar, multiple scans could be used to study the 3D evolution of the circulations, especially convergence and storm structure. The first radar observations from the S-band dual-polarised radar in Mwanza (southern shore of Lake Victoria) operated by the Tanzania Meteorological Agency have been presented by Waniha *et al.* (2019), demonstrating the utility of the radar to identify convergence lines over the lake.

In addition to more observations, idealised modelling will be a useful tool to study the moisture bulge during the early morning. Simulations of land breeze collisions under different environmental conditions – such as environmental humidity, prevailing wind and land–lake temperature contrasts – could be used to understand the formation of the bulge, as well as conditions under which it contributes to storm formation over Lake Victoria. While the propagation of the bulge feature observed and simulated during HyVic appears to be controlled by wave dynamics, the behaviour of the bulge in W19 shows more connection to density current dynamics. Idealised modelling could help understand the differences leading to these two scenarios and likely identify additional scenarios. It has been shown that even high-resolution models struggle to correctly simulate the wind, moisture and temperature gradients across the LBF. It is important to understand how this gradient may affect the known triggering of storms within the convergence zone of the LBF. Idealised modelling could also address this question by performing simulations with different horizontal grid-spacings, or by artificially imposing synoptic conditions or lake–land contrasts to change the strength of the LBF. Model runs could also be performed with and without orography to better understand the effect of orography on the lake and land breezes. While this has been done in coarser climate models (e.g., Mukabana and Pielke, 1996; Song *et al.*, 2004; Anyah *et al.*, 2006), this has not been done in a CP model.

Given the devastating impacts of storm occurrence over the lake, improving understanding of the processes responsible for storm initiation is key to improving safety on the lake. Confidence in the representation of the lake–land breeze circulation and its impacts on rainfall in climate models is also vital for planning lake management scenarios in the future (Vanderkelen *et al.*, 2018a; 2018b). The HyVic pilot flight campaign has provided observations of the underlying lake–land breeze circulation in unprecedented detail, but an extended campaign is necessary for better statistics and greater observational coverage. In particular, it remains unclear how properties of the LBF and nocturnal moisture bulge may vary on seasonal and synoptic time-scales, and how such variations may lead to deep convection; therefore ongoing observations are required throughout the year.

AUTHOR CONTRIBUTIONS


Beth J. Woodhams: conceptualization; formal analysis; investigation; methodology; visualization; writing – original draft. **Paul A. Barrett:** funding acquisition; investigation; methodology; project administration; writing – review and editing. **John H. Marsham:** conceptualization; funding acquisition; methodology; supervision; writing – review and editing. **Cathryn E. Birch:** conceptualization; funding acquisition; methodology; project administration; supervision; writing – review and editing. **Caroline L. Bain:** conceptualization; funding acquisition; methodology; project administration; resources; supervision; writing – review and editing. **Jennifer K. Fletcher:** investigation; methodology; writing – review and editing. **Andrew J. Hartley:** conceptualization; investigation; methodology; project administration; writing – review and editing. **Stuart Webster:** writing – review and editing. **Solomon Mangeni:** project administration; writing – review and editing.

ACKNOWLEDGEMENTS


The HyVic pilot flight campaign was only possible because of true collaboration and cooperation between a multitude of projects and funding bodies. Many thanks to the principal investigators of the various projects involved for working together to deliver the campaign at such low cost. Airborne data were obtained using the BAe-146-301 Atmospheric Research Aircraft (ARA) flown by Airtask Ltd and managed by FAAM Airborne Laboratory, jointly operated by UK Research and Innovation (UKRI) and the University of Leeds. Many thanks to various members of FAAM for their help and guidance during the campaign, and in particular to Hannah Price for her assistance with data post-campaign. Flight hours were provided by the National Centre for Atmospheric Science (NCAS) and the


UK Met Office. This research was conducted with financial support from UKAID under the WISER Programme through the HIGHWAY (HIGH impact Weather LAke sYstem) Project. The HIGHWAY project is an international collaboration led by the WMO, in cooperation with Kenya Meteorological Department, Meteo Rwanda, Uganda National Meteorological Authority, Tanzanian Meteorological Agency, UK Met Office and the US National Centre for Atmospheric Research. This work was also supported by UKRI as part of the Global Challenges Research Fund, grant NE/P021077/1 (GCRF African SWIFT), including time for Woodhams, Marsham, Birch, Bain, Fletcher and Webster. This work was also supported by the UK Department for International Development (DFID)/Natural Environment Research Council (NERC) Future Climate for Africa (FCFA) HyCRISTAL project (NE/M019985/1). Woodhams was also supported by the NERC SPHERES DTP (NE/L002574/1). Marsham was also supported by the National Centre for Atmospheric Science via the NERC/GCRF programme ACREW (Atmospheric hazard in developing Countries: Risk assessment and Early Warning; NE/R000034/1). Thanks are owed to Festus Luboyera and others at Uganda National Meteorological Authority (UNMA) for their hard work in ensuring HyVic could take place. Thanks and credit to the NERC Methane Observations and Yearly Assessments (MOYA) – the Global Methane Budget project (NE/N016211/1) for funding the transits and supporting HyVic as an addition to their campaign. Thanks are also owed to Declan Finney and Dean Walker for their forecast support from the UK, and Sam Clarke and others for their forecast support from the SWIFT testbed 1a held at Kenya Meteorological Department. Finally, thanks are due to Thorwald Stein and Andrew Ross for their helpful comments on the paper during Woodhams' PhD viva and to the anonymous reviewers for improving the content and clarity of the paper. ERA5 data were generated using Copernicus Climate Change Service Information (2020). Neither the European Commission nor ECMWF are responsible for any use that may be made of the Copernicus Information or data in this publication. Thank you to Richard Keane for downloading these data. The GPM IMERG data were provided by the NASA Goddard Space Flight Center's Precipitation Measurement Mission's Science Team and Precipitation Processing System, which develop and compute the GPM IMERG as a contribution to GPM, including data archiving at the NASA GES DISC. This project used the MetPy package developed by UCAR/Unidata (May *et al.*, 2008).

ORCID


Beth J. Woodhams  <https://orcid.org/0000-0003-2070-8279>


Paul A. Barrett  <https://orcid.org/0000-0002-3763-0909>

John H. Marsham  <https://orcid.org/0000-0003-3219-8472>

Cathryn E. Birch  <https://orcid.org/0000-0001-9384-2810>

Caroline L. Bain  <https://orcid.org/0000-0002-2993-9308>

Jennifer K. Fletcher  <https://orcid.org/0000-0002-4892-3344>

Andrew J. Hartley  <https://orcid.org/0000-0002-1905-9112>

REFERENCES

- Alexander, L.S., Sills, D.M.L. and Taylor, P.A. (2018) Initiation of convective storms at low-level mesoscale boundaries in southwestern Ontario. *Weather and Forecasting*, 33(2), 583–598.
- Anyah, R.O., Semazzi, F.H.M. and Xie, L. (2006) Simulated physical mechanisms associated with climate variability over Lake Victoria Basin in East Africa. *Monthly Weather Review*, 134(12), 3588–3609.
- Arritt, R.W. (1993) Effects of the large-scale flow on characteristic features of the sea breeze. *Journal of Applied Meteorology*, 32(1), 116–125.
- Asefi-Najafabady, S., Knupp, K., Mecikalski, J.R., Welch, R.M. and Phillips, D. (2010) Ground-based measurements and dual-Doppler analysis of 3-D wind fields and atmospheric circulations induced by a meso- γ -scale inland lake. *Journal of Geophysical Research: Atmospheres*, 115(D23). <https://doi.org/10.1029/2010JD014022>
- Ba, M.B. and Nicholson, S.E. (1998) Analysis of convective activity and its relationship to the rainfall over the Rift Valley lakes of East Africa during 1983–90 using the Meteosat infrared channel. *Journal of Applied Meteorology*, 37(10), 1250–1264.
- Ballentine, R.J. (1982) Numerical simulation of land-breeze-induced snowbands along the western shore of Lake Michigan. *Monthly Weather Review*, 110(11), 1544–1553.
- Barker, P.A., Allen, G., Gallagher, M., Pitt, J.R., Fisher, R.E., Bannan, T., Nisbet, E.G., Bauguitte, S.J.-B., Pasternak, D., Cliff, S., Schimpf, M.B., Mehra, A., Bower, K.N., Lee, J.D., Coe, H. and Percival, C.J. (2020) Airborne measurements of fire emission factors for African biomass burning sampled during the MOYA Campaign. *Atmospheric Chemistry and Physics*, 20, 15443–15459. <https://doi.org/10.5194/acp-20-15443-2020>.
- Beswick, K.M., Gallagher, M.W., Webb, A.R., Norton, E.G. and Perry, F. (2008) Application of the Aventech AIMMS20AQ airborne probe for turbulence measurements during the Convective Storm Initiation Project. *Atmospheric Chemistry and Physics*, 8(17), 5449–5463. <https://doi.org/10.5194/acp-8-5449-2008>.
- Biggs, W.G. and Graves, M.E. (1962) A lake breeze index. *Journal of Applied meteorology*, 1(4), 474–480.
- Bischoff-Gauss, I., Kalthoff, N. and Fiebig-Wittmaack, M. (2006) The influence of a storage lake in the Arid Elqui Valley in Chile on local climate. *Theoretical and Applied Climatology*, 85(3), 227–241.
- Boutle, I.A., Eyre, J.E. and Lock, A.P. (2014) Seamless stratocumulus simulation across the turbulent gray zone. *Monthly Weather Review*, 142(4), 1655–1668.
- Bush, M., Allen, T., Bain, C., Boutle, I.A., Edwards, J., Finnenkoetter, A., Franklin, C., Hanley, K.E., Lean, H., Lock, A.P., Manners, J., Mittermaier, M., Morcrette, C.J., North, R., Petch, J., Short, C., Vosper, S.B., Walters, D., Webster, S., Weeks, M., Wilkinson, J., Wood, N. and Zerroukat, M. (2019) The first Met Office Unified Model/JULES Regional Atmosphere and Land configuration, RAL1. *Geoscientific Model Development*, 13, 1999–2029. <https://doi.org/10.5194/gmd-13-1999-2020>.
- Camberlin, P., Gitau, W., Planchon, O., Dubreuil, V., Funatsu, B.M. and Philippon, N. (2018) Major role of water bodies on diurnal precipitation regimes in Eastern Africa. *International Journal of Climatology*, 38(2), 613–629.
- Cannon, T., Krüger, F., Bankoff, G. and Schipper, L. (2014). Putting culture at the centre of risk reduction, Chapter 7 in World Disasters Report 2014: Focus on Culture and Risk, editor=Cannon, T., editor=Schipper, L. Geneva, Switzerland: International Federation of Red Cross and Red Crescent Societies.
- Chamberlain, J.M., Bain, C.L., Boyd, D.F.A., McCourt, K., Butcher, T. and Palmer, S. (2014) Forecasting storms over Lake Victoria using a high-resolution model. *Meteorological Applications*, 21(2), 419–430.
- Comer, N.T. and McKendry, I.G. (1993) Observations and numerical modelling of Lake Ontario breezes. *Atmosphere-Ocean*, 31(4), 481–499.
- C3S (2017). ERA5: Fifth generation of ECMWF atmospheric re-analyses of the global climate. Copernicus Climate Change Service, Climate Data Store (CDS). Available at: <https://cds.climate.copernicus.eu/cdsapp#!/home>; accessed 28 August 2021.
- Crosman, E.T. and Horel, J.D. (2010) Sea and lake breezes: a review of numerical studies. *Boundary-Layer Meteorology*, 137(1), 1–29.
- Crosman, E.T. and Horel, J.D. (2012) Idealized large-eddy simulations of sea and lake breezes: sensitivity to lake diameter, heat flux and stability. *Boundary-Layer Meteorology*, 144(3), 309–328.
- Curry, M., Hanesiak, J., Kehler, S., Sills, D.M.L. and Taylor, N.M. (2017) Ground-based observations of the thermodynamic and kinematic properties of lake-breeze fronts in southern Manitoba, Canada. *Boundary-Layer Meteorology*, 163(1), 143–159.
- Datta, R.R. (1981). Certain aspects of monsoonal precipitation dynamics over Lake Victoria, pp. 333–349 in Monsoon Dynamics, editor=Lighthill, J., editor=Pearce, R.P. Cambridge, UK: Cambridge University Press.
- Dehghan, A., Mariani, Z., Leroyer, S., Sills, D., Bélair, S. and Joe, P. (2018) Evaluation of modeled lake breezes using an enhanced observational network in southern Ontario: case studies. *Journal of Applied Meteorology and Climatology*, 57(7), 1511–1534.
- Estoque, M.A. (1962) The sea breeze as a function of the prevailing synoptic situation. *Journal of the Atmospheric Sciences*, 19(3), 244–250.
- Estoque, M.A. (1981) Further studies of a lake breeze. Part I: observational study. *Monthly Weather Review*, 109(3), 611–618.
- Estoque, M.A. and Gross, J.M. (1981) Further studies of a lake breeze. Part II: theoretical study. *Monthly Weather Review*, 109(3), 619–634.
- Fiedler, E.K., Martin, M.J. and Roberts-Jones, J. (2014) An operational analysis of lake surface water temperature. *Tellus A*, 66(1). <https://doi.org/10.3402/tellusa.v66.21247>.
- Fiedler, S., Schepanski, K., Heinold, B., Knippertz, P. and Tegen, I. (2013) Climatology of nocturnal low-level jets over North Africa and implications for modeling mineral dust emission. *Journal of Geophysical Research: Atmospheres*, 118(12), 6100–6121.
- Flohn, H. and Fraedrich, K. (1966) Tagesperiodische zirkulation und niederschlagsverteilung am Victoria-See (Ostafrika) (The daily

- periodic circulation and distribution of rainfall over Lake Victoria, in German). *Meteorologische Rundschau*, 19(6), 157–165.
- Good, S., Fiedler, E., Mao, C., Martin, M.J., Maycock, A., Reid, R., Roberts-Jones, J., Searle, T., Waters, J., While, J. and Worsfold, M. (2020) The current configuration of the OSTIA system for operational production of foundation sea surface temperature and ice concentration analyses. *Remote Sensing*, 12(4). <https://doi.org/10.3390/rs12040720>
- Hanley, K.E., Pirret, J.S.R., Bain, C.L., Hartley, A.J., Lean, H.W., Webster, S. and Woodhams, B.J. (2021) Assessment of convection-permitting versions of the Unified Model over the Lake Victoria basin region. *Quarterly Journal of the Royal Meteorological Society*, 147, 1642–1660.
- Hastings, D.A. and Dunbar, P.K. (1999) Global Land One-kilometer Base Elevation (GLOBE) digital elevation model, documentation, volume 1.0. Key to Geophysical Records Documentation (KGRD) no. 34, National Oceanic and Atmospheric Administration, National Geophysical Data Center. Available at: <https://repository.library.noaa.gov/view/noaa/13424>; accessed 28 August 2021.
- Hersbach, H., Bell, B., Berrisford, P., Hirahara, S., Horányi, A., Muñoz-Sabater, J., Nicolas, J., Peubey, C., Radu, R., Schepers, D., Simmons, A., Soci, C., Abdalla, S., Abellan, X., Balsamo, G., Bechtold, P., Biavati, G., Bidlot, J., Bonavita, M., De Chiara, G., Dahlgren, P., Dee, D.P., Diamantakis, M., Dragani, R., Flemming, J., Forbes, R., Fuentes, M., Geer, A.J., Haimberger, L., Healy, S., Hogan, R.J., Hólm, E.V., Janisková, M., Keeley, S., Laloyaux, P., Lopez, P., Lupu, C., Radnoti, G., de Rosnay, P., Rozum, I., Vamborg, F., Villaume, S. and Thépaut, J.-N. (2020) The ERA5 global reanalysis. *Quarterly Journal of the Royal Meteorological Society*, 146, 1999–2049. <https://doi.org/10.1002/qj.3803>
- Hogan, E., Shelly, A. and Xavier, P. (2015) The observed and modelled influence of the Madden–Julian Oscillation on East African rainfall. *Meteorological Applications*, 22(3), 459–469.
- Holtzlag, A.A.M., Svensson, G., Baas, P., Basu, S., Beare, B., Beljaars, A.C.M., Bosveld, F.C., Cuxart, J., Lindvall, J., Steeneveld, G.J., Tjernström, M. and Van De Wiel, B.J.H. (2013) Stable atmospheric boundary layers and diurnal cycles: challenges for weather and climate models. *Bulletin of the American Meteorological Society*, 94(11), 1691–1706.
- Huffman, G.J., Bolvin, D.T., Braithwaite, D., Hsu, K., Joyce, R., Kidd, C., Nelkin, E.J., Sorooshian, S., Tan, J. and Xie, P. (2019a). Algorithm Theoretical Basis Document (ATBD) version 06. NASA Global Precipitation Measurement (GPM) Integrated Multi-satellitE Retrievals for GPM (IMERG). Available at: <https://gpm.nasa.gov/resources/documents/algorithm-information/IMERG-V06-ATBD>; accessed 28 August 2021.
- Huffman, G.J., Stocker, E.F., Bolvin, D.T., Nelkin, E.J. and Tan, J. (2019b). GPM IMERG Final Precipitation L3 Half Hourly 0.1 degree x 0.1 degree V06 (GPM_3IMERGHH), Goddard Earth Sciences Data and Information Services Center (GES DISC), Greenbelt, MD. Available at: https://disc.gsfc.nasa.gov/datasets/GPM_3IMERGHH_06/summary; accessed 28 August 2021.
- Hughes, M., Hall, A. and Fovell, R.G. (2009) Blocking in areas of complex topography, and its influence on rainfall distribution. *Journal of the Atmospheric Sciences*, 66(2), 508–518.
- Iakunin, M., Salgado, R. and Potes, M. (2018) Breeze effects at a large artificial lake: summer case study. *Hydrology and Earth System Sciences*, 22(10), 5191–5210.
- Jiang, Q. (2003) Moist dynamics and orographic precipitation. *Tellus A: Dynamic Meteorology and Oceanography*, 55(4), 301–316.
- Keen, C.S. and Lyons, W.A. (1978) Lake/land breeze circulations on the western shore of Lake Michigan. *Journal of Applied Meteorology and Climatology*, 17(12), 1843–1855.
- Kehler, S., Hanesiak, J., Curry, M., Sills, D. and Taylor, N. (2016) High Resolution Deterministic Prediction System (HRDPS) simulations of Manitoba lake breezes. *Atmosphere-Ocean*, 54(2), 93–107.
- Koseki, S. and Mooney, P.A. (2019) Influences of Lake Malawi on the spatial and diurnal variability of local precipitation. *Hydrology and Earth System Sciences*, 23(7), 2795–2812.
- Laird, N.F., Kristovich, D.A.R., Liang, X.-Z., Arritt, R.W. and Labas, K. (2001) Lake Michigan lake breezes: climatology, local forcing, and synoptic environment. *Journal of Applied Meteorology*, 40(3), 409–424.
- Lock, A.P., Brown, A.R., Bush, M.R., Martin, G.M. and Smith, R.N.B. (2000) A new boundary-layer mixing scheme. Part I: Scheme description and single-column model tests. *Monthly Weather Review*, 128(9), 3187–3199.
- Lumb, F.E. (1970) Topographic influences on thunderstorm activity near Lake Victoria. *Weather*, 25(9), 404–410.
- Lyons, W.A. (1972) The climatology and prediction of the Chicago lake breeze. *Journal of Applied Meteorology*, 11(8), 1259–1270.
- Lyons, W.A. and Olsson, L.E. (1973) Detailed mesometeorological studies of air pollution dispersion in the Chicago lake breeze. *Monthly Weather Review*, 101(5), 387–403.
- Mahony, J., Dyer, E. and Washington, R. (2021) The precipitation patterns and atmospheric dynamics of the Serengeti National Park. *International Journal of Climatology*, 41, E2051–E2072.
- Mak, M.K. and Walsh, J.E. (1976) On the relative intensities of sea and land breezes. *Journal of the Atmospheric Sciences*, 33(2), 242–251.
- Markowski, P. and Richardson, Y. (2010) *Mesoscale Meteorology in Midlatitudes*. Chichester, UK: John Wiley & Sons.
- May, R.M., Arms, S.C., Marsh, P., Bruning, E., Leeman, J.R., Goebbert, K., Thielen, J.E. and Bruick, Z.S. (2008). MetPy: A Python Package for Meteorological Data, version 0.4.3. <https://github.com/Unidata/MetPy>; accessed 28 August 2021.
- Miller, S.T.K., Keim, B.D., Talbot, R.W. and Mao, H. (2003) Sea breeze: structure, forecasting, and impacts. *Reviews of Geophysics*, 41(3)
- Milton, S.F., Diongue-Niang, A., Lamptey, B., Bain, C.L. and Birch, C.E. (2017). Numerical Weather Prediction over Africa, pp. 380–422 in *Meteorology of Tropical West Africa: The Forecasters Handbook*, editors=Parker, D.J., editors=Diop-Kane, M. Chichester, UK: John Wiley & Sons.
- Mirza, A.K., Ballard, S.P., Dance, S.L., Maisey, P., Rooney, G.G. and Stone, E.K. (2016) Comparison of aircraft-derived observations with in situ research aircraft measurements. *Quarterly Journal of the Royal Meteorological Society*, 142, 2949–2967.
- Moroz, W.J. (1967) A lake breeze on the eastern shore of Lake Michigan: observations and model. *Journal of Atmospheric Sciences*, 24(4), 337–355.
- Mukabana, J.R. and Pielke, R.A. (1996) Investigating the influence of synoptic-scale monsoonal winds and mesoscale circulations on diurnal weather patterns over Kenya using a mesoscale numerical model. *Monthly Weather Review*, 124(2), 224–244.

- Neumann, J. and Mahrer, Y. (1975) A theoretical study of the lake and land breezes of circular lakes. *Monthly Weather Review*, 103(6), 474–485.
- Okeyo, A.E. (1986) The impact of Lake Victoria on the convective activities over the Kenya Highlands. *Journal of the Meteorological Society of Japan. Series II*, 64, 689–695.
- Passarelli, R.E. and Braham, R.R. (1981) The role of the winter land breeze in the formation of Great Lake snow storms. *Bulletin of the American Meteorological Society*, 62(4), 482–491.
- Petersen, G.N. and Renfrew, I.A. (2009) Aircraft-based observations of air–sea fluxes over Denmark Strait and the Irminger Sea during high wind speed conditions. *Quarterly Journal of the Royal Meteorological Society*, 135, 2030–2045.
- Physick, W. (1976) A numerical model of the sea-breeze phenomenon over a lake or gulf. *Journal of Atmospheric Sciences*, 33(11), 2107–2135.
- Pielke, R.A. and Segal, M. (1986). Mesoscale circulations forced by differential terrain heating, pp. 516–548 in *Mesoscale Meteorology and Forecasting*, editor=Ray, P.S. Berlin: Springer.
- Pohl, B. and Camberlin, P. (2006a) Influence of the Madden–Julian Oscillation on East African rainfall. Part I: intraseasonal variability and regional dependency. *Quarterly Journal of the Royal Meteorological Society*, 132, 2521–2539.
- Pohl, B. and Camberlin, P. (2006b) Influence of the Madden–Julian Oscillation on East African rainfall. Part II: March–May season extremes and interannual variability. *Quarterly Journal of the Royal Meteorological Society*, 132, 2541–2558.
- Purificação, C., Potes, M., Rodrigues, G., Salgado, R. and Costa, M.J. (2021) Lake and land breezes at a Mediterranean artificial lake: observations in Alqueva Reservoir, Portugal. *Atmosphere*, 12(5). <https://doi.org/10.3390/atmos12050535>
- Roebber, P.J. and Gehring, M.G. (2000) Real-time prediction of the lake breeze on the western shore of Lake Michigan. *Weather and Forecasting*, 15(3), 298–312.
- Sandu, I., Beljaars, A., Bechtold, P., Mauritsen, T. and Balsamo, G. (2013) Why is it so difficult to represent stably stratified conditions in numerical weather prediction (NWP) models?. *Journal of Advances in Modeling Earth Systems*, 5(2), 117–133.
- Schmetz, J., Pili, P., Tjemkes, S., Just, D., Kerkmann, J., Rota, S. and Ratier, A. (2002) An introduction to Meteosat second generation (MSG). *Bulletin of the American Meteorological Society*, 83(7), 977–992.
- Segal, M., Leuthold, M., Arritt, R.W., Anderson, C. and Shen, J. (1997) Small lake daytime breezes: some observational and conceptual evaluations. *Bulletin of the American Meteorological Society*, 78(6), 1135–1148.
- Semazzi, F.H.M. (2011). Enhancing safety of navigation and efficient exploitation of natural resources over Lake Victoria and its basin by strengthening meteorological services on the lake. *North Carolina State University Climate Modeling Laboratory Tech. Rep*, 104.
- Sills, D.M.L., Brook, J.R., Levy, I., Makar, P.A., Zhang, J. and Taylor, P.A. (2011) Lake breezes in the southern Great Lakes region and their influence during BAQS-Met 2007. *Atmospheric Chemistry and Physics*, 11(15), 7955–7973.
- Simpson, J.E., Mansfield, D.A. and Milford, J.R. (1977) Inland penetration of sea-breeze fronts. *Quarterly Journal of the Royal Meteorological Society*, 103, 47–76.
- Smagorinsky, J. (1963) General circulation experiments with the primitive equations: I. The basic experiment. *Monthly Weather Review*, 91(3), 99–164.
- Song, Y., Semazzi, F.H.M., Xie, L. and Ogallo, L.J. (2004) A coupled regional climate model for the Lake Victoria basin of East Africa. *International Journal of Climatology*, 24(1), 57–75.
- Steenburgh, W.J., Halvorson, S.F. and Onton, D.J. (2000) Climatology of lake-effect snowstorms of the Great Salt Lake. *Monthly Weather Review*, 128(3), 709–727.
- Stivari, S.M.S., de Oliveira, A.P., Karam, H.A. and Soares, J. (2003) Patterns of local circulation in the Itaipu Lake area: numerical simulations of lake breeze. *Journal of Applied Meteorology*, 42(1), 37–50.
- Suresh, R. (2007) Observation of sea-breeze front and its induced convection over Chennai in southern peninsular India using Doppler weather radar. *Pure and Applied Geophysics*, 164, 1511–1525.
- Thiery, W., Davin, E.L., Panitz, H.-J., Demuzere, M., Lhermitte, S. and Van Lipzig, N. (2015) The impact of the African Great Lakes on the regional climate. *Journal of Climate*, 28(10), 4061–4085.
- Tsujimoto, K. and Koike, T. (2013) Land–lake breezes at low latitudes: the case of Tonle Sap Lake in Cambodia. *Journal of Geophysical Research: Atmospheres*, 118(13), 6970–6980.
- Van de Walle, J., Thiery, W., Brousse, O., Souverijns, N., Demuzere, M. and van Lipzig, N.P.M. (2020) A convection-permitting model for the Lake Victoria Basin: evaluation and insight into the mesoscale versus synoptic atmospheric dynamics. *Climate Dynamics*, 54(3), 1779–1799.
- Vance, A.K., Abel, S.J., Cotton, R.J. and Woolley, A.M. (2015) Performance of WVSS-II hygrometers on the FAAM research aircraft. *Atmospheric Measurement Techniques*, 8(3), 1617–1625.
- Vanderkelen, I., van Lipzig, N.P.M. and Thiery, W. (2018a) Modelling the water balance of Lake Victoria (East Africa) – Part 1: observational analysis. *Hydrology and Earth System Sciences*, 22(10), 5509–5525.
- Vanderkelen, I., van Lipzig, N.P.M. and Thiery, W. (2018b) Modelling the water balance of Lake Victoria (East Africa) – Part 2: future projections. *Hydrology and Earth System Sciences*, 22(10), 5527–5549.
- Wang, C., Kirshbaum, D.J. and Sills, D.M.L. (2019) Convection initiation aided by lake-breeze convergence over the Niagara Peninsula. *Monthly Weather Review*, 147(11), 3955–3979.
- Wang, Y., Gao, Y., Qin, H., Huang, J., Liu, C., Hu, C., Wang, W., Liu, S. and Lee, X. (2017) Spatiotemporal characteristics of lake breezes over Lake Taihu, China. *Journal of Applied Meteorology and Climatology*, 56(7), 2053–2065.
- Waniha, P.F., Roberts, R.D., Wilson, J.W., Kijazi, A. and Katole, B. (2019) Dual-polarization radar observations of deep convection over Lake Victoria basin in East Africa. *Atmosphere*, 10(11). <https://doi.org/10.3390/atmos10110706>
- Wexler, R. (1946) Theory and observations of land and sea breezes. *Bulletin of the American Meteorological Society*, 27(6), 272–287.
- Wood, N., Staniforth, A., White, A.A., Allen, T., Diamantakis, M., Gross, M., Melvin, T., Smith, C., Vosper, S.B., Zerroukat, M. and Thuburn, J. (2014) An inherently mass-conserving semi-implicit semi-Lagrangian discretization of the deep-atmosphere global non-hydrostatic equations. *Quarterly Journal of the Royal Meteorological Society*, 140, 1505–1520.

- Woodhams, B.J., Birch, C.E., Marsham, J.H., Bain, C.L., Roberts, N.M. and Boyd, D.F.A. (2018) What is the added value of a convection-permitting model for forecasting extreme rainfall over tropical East Africa? *Monthly Weather Review*, 146(9), 2757–2780.
- Woodhams, B.J., Birch, C.E., Marsham, J.H., Lane, T.P., Bain, C.L. and Webster, S.T. (2019) Identifying key controls on storm formation over the Lake Victoria basin. *Monthly Weather Review*, 147(9), 3365–3390.
- Xu, L., Liu, H., Du, Q., Wang, L., Yang, L. and Sun, J. (2019) Differences of atmospheric boundary-layer characteristics between pre-monsoon and monsoon period over the Erhai Lake. *Theoretical and Applied Climatology*, 135(1), 305–321.
- Yang, W., Seager, R., Cane, M.A. and Lyon, B. (2015) The annual cycle of East African precipitation. *Journal of Climate*, 28(6), 2385–2404.
- Yin, X. and Nicholson, S.E. (1998) The water balance of Lake Victoria. *Hydrological Sciences Journal*, 43(5), 789–811.
- Zerroukat, M. and Shipway, B.J. (2017) ZLF (Zero Lateral Flux): a simple mass conservation method for semi-Lagrangian-based limited-area models. *Quarterly Journal of the Royal Meteorological Society*, 143, 2578–2584.
- Zou, H., Zhang, S., Liu, Y., Zhang, W. and Yang, X. (2020) Analysis of a convective storm crossing Poyang Lake in China. *Journal of Meteorological Research*, 34(3), 529–545.
- Zumpfe, D.E. and Horel, J.D. (2007) Lake-breeze fronts in the Salt Lake Valley. *Journal of Applied Meteorology and Climatology*, 46(2), 196–211.

How to cite this article: Woodhams, B.J., Barrett, P.A., Marsham, J.H., Birch, C.E., Bain, C.L., Fletcher, J.K. *et al.* (2022) Aircraft observations and sub-km modelling of the lake–land breeze circulation over Lake Victoria. *Quarterly Journal of the Royal Meteorological Society*, 148(743), 557–580. Available from: <https://doi.org/10.1002/qj.4155>